

Please cite the Published Version

Wang, Weizhuo  (2025) Integrating data-driven reduced order models with Kriging for efficient sensor placement and full-field prediction. Mechanical Systems and Signal Processing, 234. 112760 ISSN 0888-3270

DOI: <https://doi.org/10.1016/j.ymssp.2025.112760>

Publisher: Elsevier

Version: Published Version

Downloaded from: <https://e-space.mmu.ac.uk/639569/>

Usage rights:  [Creative Commons: Attribution 4.0](https://creativecommons.org/licenses/by/4.0/)

Additional Information: This is an open access article published in Mechanical Systems and Signal Processing, by Elsevier.

Data Access Statement: Data will be made available on request.

Enquiries:

If you have questions about this document, contact openresearch@mmu.ac.uk. Please include the URL of the record in e-space. If you believe that your, or a third party's rights have been compromised through this document please see our Take Down policy (available from <https://www.mmu.ac.uk/library/using-the-library/policies-and-guidelines>)



Integrating data-driven reduced order models with Kriging for efficient sensor placement and full-field prediction

Weizhuo Wang 

Department of Engineering, Manchester Metropolitan University, Manchester, M1 5GD, UK

ARTICLE INFO

Communicated by H. Ouyang

Keywords:

Full-field displacement measurement
Adaptive Geometric Moment Descriptor
Kriging
Modal order reduction
Sparse sensor placement
Uncertainty quantification
Digital Image Correlation

ABSTRACT

This paper presents a two-stage methodology for efficient and accurate full-field displacement reconstruction using sparse online measurements derived from high-resolution Digital Image Correlation (DIC) data. The proposed approach integrates Modal Order Reduction and Kriging-based Uncertainty Quantification to address challenges associated with high-dimensional data analysis in structural dynamics.

In the offline stage, Adaptive Geometric Moment Descriptor (AGMD)-based shape features are used to compress the high-dimensional dataset, identify modal properties, and estimate residual covariance structures. In the online stage, a sparse set of optimally placed sensors, determined via QR decomposition with pivoting, is employed to infer full-field responses through *Kriging interpolation*, which also provides predictive variances for uncertainty quantification.

The methodology was demonstrated on a curved plate under random excitation. The results show strong correlations between measured and reconstructed fields using AGMDs and successfully identify multiple full-field vibration modes. In the online stage, the Kriging-predicted full-field responses, informed by an empirically estimated covariance structure from the offline dataset, exhibited better accuracy compared to predictions made using the Generalised Least Squares method (GLS). Validation on temporal sampling data achieved a coverage probability of 94.34% at 95% confidence intervals, highlighting the method's reliability and robustness.

1. Introduction

In structural health monitoring (SHM) [1–8] and structural dynamic model updating [9–11], obtaining reliable, high-resolution, full-field displacement and strain data is desirable for accurately analysing structural behaviour under diverse loading conditions. Techniques such as Digital Image Correlation (DIC) and advanced optical measurement systems [12,13] have revolutionised the validation and assessment of structural models, though they also introduce challenges including high data dimensionality, noise interference, and the need for efficient model updating strategies to ensure precise structural identification and performance predictions [6,14–17].

Mottershead and colleagues highlighted the potential of frequency response functions derived from shape features [18,19] to handle high-dimensional raw data from high-speed DIC. These shape features enable a reduced yet representative set of coordinates for the high-resolution dynamic responses, which is particularly advantageous in digital twinning applications where a fast, efficient, and data-driven model is desired for real-time monitoring [20–22].

Several recent approaches have been proposed in the literature to address the challenge of reconstructing high-fidelity dynamic responses from sparse structural health monitoring data. For instance, Zhang XH and colleagues [23] employs a KLT-QR-based

E-mail address: w.wang@mmu.ac.uk.

<https://doi.org/10.1016/j.ymssp.2025.112760>

Received 18 December 2024; Received in revised form 9 March 2025; Accepted 13 April 2025

Available online 2 May 2025

0888-3270/© 2025 The Author. Published by Elsevier Ltd. This is an open access article under the CC BY license (<http://creativecommons.org/licenses/by/4.0/>).

measurement matrix optimisation to enhance the accuracy of dynamic response reconstruction from limited measurements, whereas Zhang Y and colleagues [24] introduce a compressive sensing framework under dictionary learning that first obtains dense, controlled data and then solves a sparse binary multi-objective optimisation problem for sensor placement and damage detection. Jana Debasish and Nagarajaiah [17] propose a framework for full-field online sensing in the spatial domain, learning dictionary-based mode shapes for linear time-invariant systems and estimating the minimal number of sensors via singular value decomposition.

Compared with these compressive sensing and dictionary-based methods, the current study offers a distinct, data-driven approach for full-field displacement reconstruction. Specifically, an Adaptive Geometric Moment Descriptor (AGMD) is employed to compress the high-dimensional DIC data in an offline stage, extracting modal properties and estimating empirical covariance structures without relying on finite element models or pre-trained dictionaries. A systematic sensor placement follows, using QR decomposition with pivoting, which ensures maximal linear independence for accurate sampling. Finally, a Kriging-based uncertainty quantification method predicts the full-field response and provides predictive variances, resulting in a scalable and efficient solution for structural health monitoring applications.

The present approach comprises two primary stages:

Offline Stage: Data Compression and Modal Property Identification

In the first stage, dynamic measurements obtained from DIC are processed. Given the high spatial dimensionality of DIC data, direct modal property identification can be computationally demanding. Shape feature compression techniques are applied to reduce dimensionality while preserving essential structural characteristics, facilitating efficient modal property identification.

Online Stage: Sparse Sensor Deployment and Full-Field Response Inference

The second stage introduces an online monitoring framework that utilises the modal properties and shape basis functions identified during the offline stage. A strategically deployed sparse sensor network measures responses, which are then integrated with the pre-determined shape basis functions to infer full-field responses. This strategy reduces the cost and complexity of sensor deployment while achieving reliable and accurate response reconstruction.

The remainder of the paper is structured as follows. Section 2 discusses the challenges associated with handling full-field DIC data and outlines the theoretical foundation of modal identification via shape feature compression. Section 3 presents the proposed methodology, integrating modal order reduction and Kriging-based uncertainty quantification for spatial prediction using sparse measurements. Section 4 demonstrates the effectiveness of the approach through a case study involving a curved plate. Finally, Section 5 summarises the findings and proposes directions for future research.

2. Context and background

This section delineates the methods employed in processing full-field dynamic measurements, encompassing the acquisition of displacement data through 3D stereo Digital Image Correlation, the challenges associated with traditional vibration modal identification approaches, and the application of the Adaptive Geometric Moment Descriptor for data compression and modal analysis.

2.1. 3D stereo digital image correlation measurements

3D stereo Digital Image Correlation is a non-contact optical method utilised for measuring full-field displacements and strains on the surface of objects undergoing deformation [12,13]. By capturing sequential images from multiple camera angles, 3D stereo DIC reconstructs the three-dimensional displacement vectors of a mesh comprising numerous vertices connected by triangular elements.

The displacement data acquired through 3D stereo DIC can be represented as a matrix $\mathbf{X} \in \mathbb{R}^{N_d \times N_T}$, where N_d denotes the total degrees of freedom (DOF), corresponding to the number of vertices in the triangular mesh; N_T signifies the number of temporal samples captured during dynamic measurements.

Each column of \mathbf{X} represents the displacement vectors of all N_d vertices at a specific time instance, enabling the analysis of dynamic structural behaviour over time.

2.2. Adaptive geometric moment descriptor for data compression

The AGMD provides a systematic approach for compressing high-dimensional DIC data by projecting the displacement field onto a set of orthonormal shape basis functions. This process begins with the parameterisation [25] of the measured surface (a 2-manifold obtained from DIC measurements) into a suitable 2D coordinate system (u, v) . Once this parameterisation is established, a family of bivariate monomial basis functions is constructed and orthonormalised to form a reduced representation of the displacement data.

Continuous Parameterisation and Orthogonality:

On the parameter domain $D \subset \mathbb{R}^2$, a set of bivariate monomials $\{\phi_{mn}(u, v) = u^m v^n\}$ is selected up to certain polynomial orders (m_{\max}, n_{\max}) . The continuous orthonormality condition requires that [26]:

$$\int_D \phi_i(u, v) \phi_j(u, v) du dv = \delta_{ij}, \quad (1)$$

where $\{\phi_k(u, v)\}_{k=1}^R$ are the orthonormalised shape basis functions of $\{\phi_{mn}(u, v)\}$, and $R = (m_{\max} + 1)(n_{\max} + 1)$. Here, δ_{ij} denotes the Kronecker delta.

Discrete Approximation Using a Triangular Mesh:

In practice, the measured surface \mathcal{M} is represented as a triangular mesh composed of N_d vertices $\{\mathbf{p}_i \in \mathbb{R}^3 : i = 1, 2, \dots, N_d\}$ obtained from 3D stereo DIC. Each vertex i is associated with parameters (u_i, v_i) mapping it onto \mathcal{D} . The continuous integral is then approximated by a discrete summation over the mesh nodes. To achieve a meaningful discrete approximation, a weight $w_i > 0$ is assigned to each vertex, often chosen to represent the local area associated with that vertex (e.g., by splitting each triangular element among its vertices proportionally) [27]. Thus, the orthonormality condition becomes:

$$\sum_{i=1}^{N_d} \varphi_i^{(\ell)}(u_i, v_i) \varphi_i^{(m)}(u_i, v_i) w_i = \delta_{\ell m}. \quad (2)$$

Discrete Gram–Schmidt Orthonormalisation:

Starting with the raw monomials $\{\phi_{mn}(u_i, v_i)\}$, a discrete Gram–Schmidt orthonormalisation [28] is performed:

1. Select the first monomial and normalise it:

$$\varphi_1(u_i, v_i) = \frac{\phi_{0,0}(u_i, v_i)}{\sqrt{\sum_{r=1}^{N_d} [\phi_{0,0}(u_r, v_r)]^2 w_r}}. \quad (3)$$

2. For subsequent monomials ϕ_{mn} , subtract projections onto all previously obtained orthonormal functions:

$$\tilde{\phi}_{mn}(u_i, v_i) = \phi_{mn}(u_i, v_i) - \sum_{j=1}^{k-1} \left(\sum_{r=1}^{N_d} \phi_{mn}(u_r, v_r) \varphi_j(u_r, v_r) w_r \right) \varphi_j(u_i, v_i). \quad (4)$$

3. Normalise $\tilde{\phi}_{mn}$ to obtain $\varphi_k(u_i, v_i)$.

Repeating this for all R monomials yields the orthonormal basis matrix $\Phi \in \mathbb{R}^{N_d \times R}$, whose columns correspond to the orthonormal shape basis functions, $\varphi_k(u_i, v_i)$, evaluated at the N_d vertices of the triangular mesh.

Projection and AGMD Coefficients:

Once Φ is constructed, the displacement data $\mathbf{X} \in \mathbb{R}^{N_d \times N_T}$, with N_T time samples, can be projected onto this reduced basis. Since Φ is orthonormal, the shape feature coefficients $\mathbf{B} \in \mathbb{R}^{R \times N_T}$, also termed AGMD coefficients, are obtained by:

$$\mathbf{B} = \Phi^\top \mathbf{X}. \quad (5)$$

For each temporal snapshot t :

$$\mathbf{X}_t \approx \Phi \mathbf{b}_t, \quad (6)$$

where $\mathbf{b}_t = \mathbf{B}(:, t)$.

Feature Selection and Residual Uncertainty:

To further reduce dimensionality, an ‘energy’-based criterion can be used to rank the shape features (the columns of Φ). The energy of the k th feature of \mathbf{b}_t is:

$$E_k = \sum_{t=1}^{N_T} b_{k,t}^2. \quad (7)$$

Retaining only the top $r < R$ features with the highest energy ensures that a consistent set of significant features is used across all time steps. While each time step may differ in how well it compresses to this reduced feature space, using a fixed subset of features ensures consistency.

However, reducing the dataset to r features inevitably discards some information. Quantifying the residual uncertainty that arises from this compression—especially if strain calculations or detailed dynamic analyses are required—becomes essential [29]. As the following sections will discuss, integrating a Kriging-based approach allows for the modelling of this uncertainty, ensuring that the final reconstructed fields are accompanied by reliable confidence estimates.

Data Compression and Validation

By retaining only the most significant $r \leq R$ shape features (e.g., those corresponding to the largest magnitudes or principal contributions), the AGMD effectively compresses the dataset. The compressed approximation becomes:

$$\mathbf{X} \approx \Phi_r \mathbf{B}_r, \quad (8)$$

where $\Phi_r \in \mathbb{R}^{N_d \times r}$ and $\mathbf{B}_r \in \mathbb{R}^{r \times N_T}$. The reconstruction error is assessed by comparing \mathbf{X} and its approximation $\Phi_r \mathbf{B}_r$, using measures such as the Frobenius norm of the error or the *correlation coefficient*:

$$\rho_t = \frac{\mathbf{X}_t^\top \mathbf{X}_{\text{rec},t}}{\|\mathbf{X}_t\|_2 \|\mathbf{X}_{\text{rec},t}\|_2}. \quad (9)$$

A high correlation coefficient (close to 1) and minimal error norms indicate that AGMD has effectively captured the essential spatial structure of the displacement field with a significantly reduced number of shape features [18].

It is worth noting that AGMD constructs basis functions based on the geometry of the measured domain, thereby preserving local spatial relationships essential for accurate strain evaluation. In contrast, alternative approaches, such as principal component

analysis [30,31], derive orthonormal subspaces directly from measured displacement snapshots rather than from the spatial domain, and thus do not inherently maintain spatial continuity. This limitation may introduce artificial discontinuities in strain evaluation, particularly when the dataset's coordinate ordering lacks a predefined structure. Accordingly, AGMD was selected to ensure local spatial consistency in data projection and to mitigate potential uncertainties in strain estimation when needed.

This AGMD-based compression stage lays the groundwork for efficient modal identification and subsequent online monitoring. By working with a low-dimensional representation, vibration modal characteristics (natural frequencies, mode shapes) can be extracted more efficiently, and the computational burden associated with handling massive DIC datasets is greatly alleviated.

2.3. Modal identification using shape features

Vibration modal identification methods [32,33] are crucial for characterising the dynamic behaviour of structures [34,35], including their natural frequencies, mode shapes, and damping ratios. Traditional approaches typically rely on datasets with available degrees of freedom obtained from strategically placed sensors to capture structural responses. These methods are broadly categorised into time-domain and frequency-domain techniques [36–42].

While effective for datasets with a moderate number of DOFs, the advent of full-field, high-spatial-resolution data, such as those generated by high-speed Digital Image Correlation systems, introduces significant computational challenges. High-resolution DIC data often encompass thousands of measurement points over numerous temporal steps, resulting in datasets with millions of elements. The substantial memory and processing demands make direct application of conventional modal identification methods computationally intensive or even infeasible. To overcome this, efficient data compression or reduced-order modelling techniques are essential, allowing for practical analysis of high-resolution datasets while retaining key structural characteristics and reducing computational overhead.

With the full-field DIC displacement data compressed into a lower-dimensional feature space via the AGMD, the subsequent objective is to efficiently identify the vibration modes of the structure. Building upon the compressed shape feature matrix \mathbf{B}_r , vibration modal identification is conducted to extract the dynamic characteristics of the structure. As established in the previous work with Mottershead and colleagues [18], a Shape Feature Frequency Response Function can be fitted to the compressed data.

Alternatively, the state-space formulation can be adapted to operate directly on the shape features, facilitating streamlined modal analysis [43]. This process involves applying well-established subspace identification techniques, such as the Numerical Subspace State Space System Identification (N4SID) method [32,44,45], to the feature matrix \mathbf{B}_r . This approach enables the extraction of modal parameters with significantly reduced computational effort compared to traditional methods that operate on the full-scale displacement data.

Suppose \mathbf{U} represents the identified 'shape feature' mode shapes. The full-field displacement mode shapes \mathbf{V} can then be reconstructed via:

$$\mathbf{V} \approx \Phi_r \mathbf{U} \quad (10)$$

where $\Phi_r \in \mathbb{R}^{N_d \times r}$ are a subset of the orthonormal shape basis functions derived from the AGMD; $\mathbf{U} \in \mathbb{R}^{r \times r_s}$ contains the mode shapes identified from the reduced-order shape feature space; r is the number of shape features retained in the AGMD (with $r \ll N_d$); r_s is the number of retained modes (with $r_s \leq r$).

The identified modal properties may subsequently be applied to inform the sparse sensor placement process and facilitate uncertainty quantification in the reconstruction of full-field displacements.

2.4. Sensor placement strategies and two-stage approach

In structural health monitoring and dynamic testing [2,4,46], the optimal placement of sensors is crucial for capturing the most informative data with a limited number of measurement points. While full-field measurement techniques such as 3D stereo Digital Image Correlation offer comprehensive displacement data [47–49], they are often impractical for continuous monitoring due to cost and complexity. Therefore, strategically placing a sparse array of point-wise sensors becomes essential for effective long-term monitoring.

2.4.1. Brief overview optimal sensor placement strategies

Several methodologies have been developed to address the optimal sensor placement problem, primarily focusing on maximising the information captured about the structural dynamics.

Introduced by Kammer [50], the *Effective Independence (Efi)* method optimises sensor locations by maximising the determinant of the Fisher Information Matrix (FIM). The FIM, which quantifies the information content of measurements regarding the modal parameters, may be defined as:

$$\text{FIM} = \mathbf{V}^T \mathbf{W} \mathbf{V} \quad (11)$$

where \mathbf{V} is the matrix of mode shapes; \mathbf{W} is a weighting matrix, often chosen as the inverse of the measurement noise covariance.

The Efi method iteratively selects sensor locations that contribute most significantly to the FIM, thereby ensuring independent and informative measurements. However, Efi may suffer from poor signal-to-noise ratio (SNR) if the selected locations correspond to nodes or areas with low dynamic responses [51].

Modal Assurance Criterion (MAC) assesses the linear independence between mode shapes [43,52]. The MAC value between two mode shapes \mathbf{v}_i and \mathbf{v}_j is given by:

$$\text{MAC}_{ij} = \frac{|\mathbf{v}_i^\top \mathbf{v}_j|^2}{(\mathbf{v}_i^\top \mathbf{v}_i)(\mathbf{v}_j^\top \mathbf{v}_j)} \quad (12)$$

Optimal sensor placement aims to minimise off-diagonal MAC values, ensuring that the measured modes are distinguishable. This method typically relies on mode shape information obtained from finite element models, though it can also be applied using identified full-field mode shapes.

Beyond the Efl method, other approaches directly optimise norms of the *Fisher Information Matrix*, such as its trace or eigenvalues [53]. By maximising these norms, the sensor configuration enhances the observability of the system's dynamic characteristics.

Information Entropy Methods consider the uncertainty associated with modal parameter estimation [54,55]. The objective is to minimise the entropy, defined as:

$$\mathcal{H} = - \sum_i \mathcal{P}_i \ln \mathcal{P}_i \quad (13)$$

where \mathcal{P}_i represents the probability distribution of the modal parameters. Sensor placement is optimised to reduce this uncertainty, often requiring a nominal model for estimation.

Techniques like driving point residue (DPR) and kinetic energy methods prioritise sensor locations with high dynamic responses [43]. By focusing on areas with significant kinetic energy, these methods aim to improve the SNR of measurements.

While effective, these methods often depend on accurate nominal models (e.g., FE models). Tchomodanova, Sanayei and Chatzi et al. [7] presented a method that integrates modal expansion with augmented Kalman filters for strain prediction at unmeasured locations using sparse response-only vibration measurements. The approach relies on finite element model updating for sensor placement and strain prediction, incorporating model-based assumptions and requiring batch data processing.

Yang and Ouyang [56] proposed a load-dependent sensor placement method for model updating, aimed at enhancing the accuracy of finite element analysis by optimally capturing structural responses under specific loading conditions. Their method combines generalised modal coordinates with dynamic responses, incorporates non-probabilistic uncertainty propagation, and employs multi-objective optimisation to balance deterministic and uncertain objectives effectively.

2.4.2. Data-driven sensor placement using shape features

In contrast to model-driven approaches, and inspired by the work of Manohar and Brunton et al. on data-driven methods [57,58], we adopted a data-driven approach that leverages the Adaptive Geometric Moment Descriptor and the compressed shape features \mathbf{b}_t obtained from actual measurements. The objective is to determine optimal sensor locations that enable accurate reconstruction of full-field displacements while facilitating uncertainty quantification through Kriging prediction.

Formulation:

With the tailored basis functions $\Phi_r \in \mathbb{R}^{N_d \times r}$ from the AGMD, the displacement field at time t can be approximated as:

$$\mathbf{X}_t \approx \Phi_r \mathbf{b}_t \quad (14)$$

The objective is to select p sensor locations such that the measurements $\mathbf{x}_t \in \mathbb{R}^p$ provide sufficient information to estimate \mathbf{b}_t . The relationship between sensor measurements and shape features is:

$$\mathbf{x}_t = \mathbf{L}_0 \mathbf{X}_t \approx \mathbf{L}_0 \Phi_r \mathbf{b}_t = \Theta \mathbf{b}_t \quad (15)$$

where $\mathbf{L}_0 \in \mathbb{R}^{p \times N_d}$ is the sensor placement matrix; $\Theta = \mathbf{L}_0 \Phi_r \in \mathbb{R}^{p \times r}$ is the reduced measurement matrix.

Another data-driven approach for creating the shape basis functions Φ is to apply Principal Component Analysis (PCA) to the entire dataset and retain the dominant principal components as the shape basis functions [17]. However, performing PCA e.g. through Singular Value Decomposition (SVD) can potentially overlook the spatial relationships inherent in the full-field data when projecting the measurements onto the space spanned by the principal components. This limitation may render the approach less desirable for applications involving strain field evaluation, where preserving spatial consistency is critical.

Optimal Sensor Placement via QR Decomposition with Pivoting:

To ensure that Θ is well-conditioned for inversion, it aims to select rows of Φ_r (i.e., sensor locations) that maximise the linear independence among the rows. This can be formulated as:

$$\xi^* = \arg \max_{\xi, |\xi|=p} \det(\Theta^\top \Theta) = \arg \max_{\xi, |\xi|=p} \prod_{i=1}^r \sigma_i^2(\Theta) \quad (16)$$

where $\sigma_i(\Theta)$ are the singular values of Θ .

QR decomposition with column pivoting is an efficient algorithm to approximate this optimisation [57,59]. The pivoting process selects rows of Φ_r that contribute most to the independence of the system, enhancing the estimation of \mathbf{b}_t .

Sensor Placement Matrix Construction:

The sensor placement matrix \mathbf{L}_0 is constructed using canonical basis vectors $\mathbf{e}_j \in \mathbb{R}^{N_d}$:

$$\mathbf{L}_0 = \begin{bmatrix} \mathbf{e}_{\xi_1}^T \\ \mathbf{e}_{\xi_2}^T \\ \vdots \\ \mathbf{e}_{\xi_p}^T \end{bmatrix} \quad (17)$$

where $\xi = \{\xi_1, \xi_2, \dots, \xi_p\}$ are the indices of the selected sensor locations.

Building upon the aforementioned sensor placement strategies, we introduce a two-stage approach that integrates modal reduction with Kriging-based uncertainty quantification to enhance full-field displacement reconstruction from sparse sensor data, as detailed in the next Section.

3. Proposed two-stage kriging prediction method

This section introduces the main contribution of this paper: a *two-stage methodology* integrating *Modal Order Reduction* and *Kriging* for spatial prediction using sparse online measurements. This approach leverages basis functions derived from a comprehensive offline dataset to efficiently model and predict spatial responses at unmeasured locations while accounting for measurement uncertainties.

3.1. Overview of the two-stage approach

The proposed method comprises two primary stages:

1. Offline Stage:

- (a) **Modal Order Reduction:** Utilise high-fidelity displacement data obtained from full-field measurements (e.g., from 3D stereo DIC) to construct a reduced-order model of the structural response using modal basis functions.
- (b) **Residual Covariance Estimation:** Estimate the covariance of the residuals not captured by the modal approximation to inform the Kriging model.

2. Online Stage:

- (a) **Measurement Acquisition and Modal Coefficient Estimation:** Collect real-time measurements from a limited number of optimally placed sensors and estimate the modal coefficients.
- (b) **Residual Prediction via Kriging:** Use Kriging interpolation to predict residuals at unmeasured locations, leveraging the spatial covariance structure estimated offline.
- (c) **Final Response Prediction:** Combine the modal approximation and predicted residuals to reconstruct the full-field displacement and quantify uncertainties.

A flowchart of the two-stage methodology is presented in Fig. 1. The offline stage, highlighted in teal boxes, focuses on data compression and modal property identification, while the online stage, shown in orange boxes, utilises the identified modal properties and shape basis functions to predict full-field responses from sparse measurements.

For a given specimen, DIC measurements can capture its topology, which serves as the foundation for extracting orthonormal basis functions. The optimal sensor placement is determined using QR decomposition with column pivoting, ensuring maximal independence among sensor locations. The displacement field is projected onto these shape features, facilitating modal property identification via N4SID. These identified modal properties enable mode shape expansion, while residual displacements are treated as a random field with an empirically estimated covariance structure. Kriging interpolation is then employed to predict full-field responses, integrating real-time sparse measurements obtained during live monitoring. The proposed approach aims to reduce the cost and complexity of sensor deployment while ensuring reliable and accurate response reconstruction. Further details are provided in the following subsections.

3.2. Stage 1: Offline stage

3.2.1. Data representation and modal order reduction

Let $\mathbf{X} \in \mathbb{R}^{N_d \times N_T}$ denote the observed displacement data across N_d DOFs over N_T time samples. Each column $\mathbf{X}_t = \mathbf{X}(:, t)$ represents the spatial response at time t .

We approximate \mathbf{X} using a set of modal basis functions (mode shapes) $\mathbf{V} \in \mathbb{R}^{N_d \times r}$ ($r \ll N_d$) as follows:

$$\mathbf{X} = \hat{\mathbf{X}} + \boldsymbol{\eta} + \boldsymbol{\epsilon} \quad (18)$$

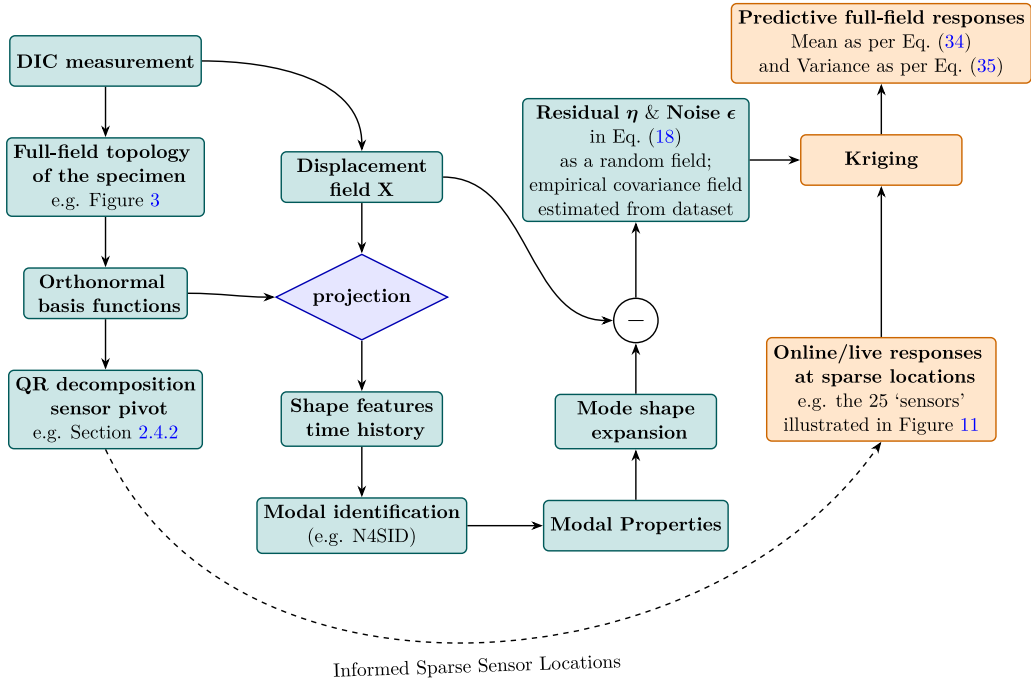


Fig. 1. A flowchart illustrating the two-stage methodology for full-field displacement reconstruction using sparse measurements.

where $\hat{\mathbf{X}} = \mathbf{V}\boldsymbol{\beta}$ is the modal approximation; $\boldsymbol{\beta} \in \mathbb{R}^{r \times N_T}$ contains the modal coefficients; $\boldsymbol{\eta} \in \mathbb{R}^{N_d \times N_T}$ captures the **residuals** not explained by the modal approximation; $\boldsymbol{\epsilon} \in \mathbb{R}^{N_d \times N_T}$ represents measurement noise.

Justification of the Formulation:

The modal shape functions \mathbf{V} are reconstructed by Eq. (10) from shape feature mode shapes \mathbf{U} obtained through standard modal identification techniques applied to the time history of shape features. They reflect the physics of the underlying structural mechanics. Specifically, $\mathbf{V} \in \mathbb{R}^{N_d \times r}$ is obtained with ($r_s \leq r \ll N_d$), where r is the number of shape features retained in the AGMD; r_s is the number of retained modes.

The *sources of approximation errors* can be categorised into two types: (1) *Shape Feature Approximation Residue*, which arises due to the dimensionality reduction in the shape feature space (from N_d to r_s), introducing inherent approximation errors; and (2) *Modal Order Truncation Residue*, which results from truncating higher-order modes in \mathbf{V} , leading to additional errors. Consequently, the residual term $\boldsymbol{\eta}$ captures the *bias* stemming from both the shape feature approximation residue and the modal order truncation residue. This term accounts for the variability in \mathbf{X} that is not captured by the modal approximation $\hat{\mathbf{X}}$.

Assumption on Measurement Noise ($\boldsymbol{\epsilon}$)

It may be assumed that the measurement noise $\boldsymbol{\epsilon}$ is independent and identically distributed (i.i.d.) Gaussian across both spatial locations and time:

$$\epsilon_{i,t} \sim \mathcal{N}(0, \sigma^2) \tag{19}$$

for $i = 1, 2, \dots, N_d$ and $t = 1, 2, \dots, N_T$.

Covariance Structure of Measurement Noise

Since $\boldsymbol{\epsilon}$ is i.i.d. across both spatial and temporal dimensions, the covariance matrix of $\boldsymbol{\epsilon}$ at a fixed time t is:

$$\text{Cov}(\boldsymbol{\epsilon}_t) = \sigma^2 \mathbf{I}_{N_d} \tag{20}$$

where \mathbf{I}_{N_d} is the identity matrix of size $N_d \times N_d$.

3.2.2. Computation of modal coefficients

The modal coefficients $\boldsymbol{\beta}$ may be determined by solving the least squares problem:

$$\min_{\boldsymbol{\beta}} \|\mathbf{X} - \mathbf{V}\boldsymbol{\beta}\|_F^2 \tag{21}$$

3.3. Residual covariance estimation

To model the residuals $\eta = \mathbf{X} - \mathbf{V}\beta$, the empirical covariance matrix may be established by [60],

$$\mathbf{C}_\eta = \frac{1}{N_T - 1} \boldsymbol{\eta} \boldsymbol{\eta}^\top \in \mathbb{R}^{N_d \times N_d} \quad (22)$$

Since the measurement noise ϵ contributes to \mathbf{C}_η , the covariance matrix needs to be adjusted to isolate the spatially correlated residuals:

$$\mathbf{C}_\eta^{\text{adjusted}} = \mathbf{C}_\eta - \hat{\sigma}^2 \mathbf{I}_{N_d} \quad (23)$$

where $\hat{\sigma}^2$ is the estimated measurement noise variance.

Estimation of Measurement Noise Variance

Assuming noise σ^2 is unknown, it may be estimated from the diagonal elements of \mathbf{C}_η [61]:

$$\hat{\sigma}^2 = \frac{1}{N_d} \sum_{i=1}^{N_d} \left(\mathbf{C}_\eta(i, i) - \sum_{k=1}^s \lambda_k \psi_k^2(i) \right) \quad (24)$$

where λ_k and $\psi_k(i)$ are the eigenvalues and eigenvectors from the PCA of $\mathbf{C}_\eta^{\text{adjusted}}$; and s is the number of principal components retained.

Extraction of Residual Basis Functions

PCA is performed on $\mathbf{C}_\eta^{\text{adjusted}}$ to obtain the residual basis functions $\boldsymbol{\Psi} \in \mathbb{R}^{N_d \times s}$ and associated variances $\boldsymbol{\Lambda} \in \mathbb{R}^{s \times s}$:

$$\mathbf{C}_\eta^{\text{adjusted}} \approx \boldsymbol{\Psi} \boldsymbol{\Lambda} \boldsymbol{\Psi}^\top \quad (25)$$

The residuals can then be approximated as [60,62]:

$$\eta \approx \boldsymbol{\Psi} \boldsymbol{\gamma} \quad (26)$$

where $\boldsymbol{\gamma} \in \mathbb{R}^{s \times N_T}$ contains the coefficients for the residual basis functions.

The number of residual basis functions s is determined by specifying a threshold for the variance explained by the principal components, for example, 99%.

The offline stage produces the necessary parameters for the online monitoring phase, including displacement modal shapes (\mathbf{V}), residual basis functions ($\boldsymbol{\Psi}$), the residual covariance matrix ($\boldsymbol{\Lambda}$), and the estimated measurement noise variance ($\hat{\sigma}^2$). These outputs are stored and subsequently utilised for accurate and efficient full-field displacement reconstruction during the online stage.

3.4. Stage 2: 'Online' stage

3.4.1. Measurement acquisition and modal coefficient estimation

During the online phase, sparse measurements $\mathbf{x}_t \in \mathbb{R}^p$ are obtained at time t from p spatial locations $\mathbf{S}_p \subseteq \{1, 2, \dots, N_d\}$. Corresponding rows of the modal basis $\mathbf{V}_p \in \mathbb{R}^{p \times r_s}$ and the residual basis $\boldsymbol{\Psi}_p \in \mathbb{R}^{p \times s}$ are extracted. The sparse sensor locations are determined using the QR decomposition method, as discussed in Section 2.4.1.

The measurement model at time t is expressed as:

$$\mathbf{x}_t = \mathbf{V}_p \boldsymbol{\beta}_t + \boldsymbol{\Psi}_p \boldsymbol{\gamma}_t + \boldsymbol{\epsilon}_t \quad (27)$$

where $\boldsymbol{\beta}_t \in \mathbb{R}^{r_s}$ are the modal coefficients at time t , $\boldsymbol{\gamma}_t \in \mathbb{R}^s$ are the residual coefficients, and $\boldsymbol{\epsilon}_t \sim \mathcal{N}(\mathbf{0}, \hat{\sigma}^2 \mathbf{I}_p)$ represents the measurement noise. Notably, the noise characteristics during the online stage are generally different from those in the offline stage (as shown in Eq. (18)), since point-wise sensors differ from DIC measurements. However, for the purpose of validating the proposed methodology in this study, the sparse sensor locations are extracted directly from the same DIC dataset and treated as equivalent to sparse point-wise sensors.

The modal coefficients $\boldsymbol{\beta}_t$ may be estimated by solving the weighted least squares problem:

$$\min_{\boldsymbol{\beta}_t} (\mathbf{x}_t - \mathbf{V}_p \boldsymbol{\beta}_t)^\top \mathbf{C}_{\text{obs}}^{-1} (\mathbf{x}_t - \mathbf{V}_p \boldsymbol{\beta}_t) \quad (28)$$

where the observed covariance matrix may be expressed as [61]:

$$\mathbf{C}_{\text{obs}} = \boldsymbol{\Psi}_p \boldsymbol{\Lambda} \boldsymbol{\Psi}_p^\top + \hat{\sigma}^2 \mathbf{I}_p \quad (29)$$

Solving the equation yields

$$\boldsymbol{\beta}_t = \left(\mathbf{V}_p^\top \mathbf{C}_{\text{obs}}^{-1} \mathbf{V}_p \right)^{-1} \mathbf{V}_p^\top \mathbf{C}_{\text{obs}}^{-1} \mathbf{x}_t \quad (30)$$

This estimation ensures that the modal coefficients account for both the modal approximation and the residual uncertainties.

3.4.2. Residual prediction via Kriging

Residuals at the sparsely measured locations may be computed by

$$\mathbf{r}_t = \mathbf{x}_t - \mathbf{V}_p \boldsymbol{\beta}_t \tag{31}$$

The residuals $\eta_{\bar{p},t}$ at unmeasured locations $\mathbf{S}_{\bar{p}} = \{1, 2, \dots, N_d\} \setminus \mathbf{S}_p$ may be approximated by Kriging prediction using the residual covariance structure estimated offline.

The joint distribution at time t may be expressed as [60,61],

$$\begin{bmatrix} \mathbf{r}_t \\ \boldsymbol{\eta}_{\bar{p},t} \end{bmatrix} \sim \mathcal{N} \left(\mathbf{0}, \begin{bmatrix} \mathbf{C}_{pp} & \mathbf{C}_{p\bar{p}} \\ \mathbf{C}_{\bar{p}p} & \mathbf{C}_{\bar{p}\bar{p}} \end{bmatrix} \right) \tag{32}$$

where $\mathbf{C}_{pp} = \boldsymbol{\Psi}_p \boldsymbol{\Lambda} \boldsymbol{\Psi}_p^T + \hat{\sigma}^2 \mathbf{I}_p$; $\mathbf{C}_{\bar{p}p} = \mathbf{C}_{pp}^T = \boldsymbol{\Psi}_{\bar{p}} \boldsymbol{\Lambda} \boldsymbol{\Psi}_p^T$; $\mathbf{C}_{\bar{p}\bar{p}} = \boldsymbol{\Psi}_{\bar{p}} \boldsymbol{\Lambda} \boldsymbol{\Psi}_{\bar{p}}^T$.

The conditional distribution may be expressed as,

$$\eta_{\bar{p},t} | \mathbf{r}_t \sim \mathcal{N} \left(\boldsymbol{\mu}_{\eta_{\bar{p},t}}, \boldsymbol{\nu}_{\eta_{\bar{p}}} \right) \tag{33}$$

where the conditional mean [60] may be expressed as,

$$\boldsymbol{\mu}_{\eta_{\bar{p},t}} = \mathbf{C}_{\bar{p}p} \mathbf{C}_{pp}^{-1} \mathbf{r}_t$$

and the conditional covariance [60] may be expressed as,

$$\boldsymbol{\nu}_{\eta_{\bar{p}}} = \mathbf{C}_{\bar{p}\bar{p}} - \mathbf{C}_{\bar{p}p} \mathbf{C}_{pp}^{-1} \mathbf{C}_{p\bar{p}}$$

3.4.3. Final response prediction

The predicted responses at unmeasured locations may be expressed as [60,61],

$$\hat{\mathbf{X}}_{\bar{p},t} = \mathbf{V}_{\bar{p}} \boldsymbol{\beta}_t + \boldsymbol{\mu}_{\eta_{\bar{p},t}} \tag{34}$$

where $\mathbf{V}_{\bar{p}} \in \mathbb{R}^{(N_d-p) \times r}$ are the modal basis functions at the unmeasured locations.

The predictive variance may be expressed as,

$$\text{Var}(\hat{\mathbf{X}}_{\bar{p},t}) = \text{diag} \left(\boldsymbol{\nu}_{\eta_{\bar{p}}} \right) \tag{35}$$

This variance quantifies the uncertainty in the predicted displacements at the unmeasured locations, which is essential for reliability assessment in structural health monitoring [8].

4. Case study: Vibration analysis of a curved plate

This case study applies the proposed two-stage methodology to the vibration analysis of a curved plate, demonstrating the effectiveness of integrating *Modal Order Reduction* and *Kriging* for full-field displacement reconstruction using sparse online measurements.

4.1. Specimen and experimental setup using DIC

As illustrated in Fig. 2, a slightly curved polypropylene (PP) plate with dimensions 260 mm × 180 mm × 3 mm was suspended using four elastic cords to simulate free boundary conditions. A stinger connected to an electrodynamic shaker induced random excitations within the frequency range of 0–512 Hz, and the corresponding force input was recorded using a force transducer.

Two high-speed CMOS cameras were employed to capture transient images of the plate at a rate of 1000 frames per second over a duration of 4 s, resulting in 4000 temporal steps. Digital Image Correlation was utilised with Dantec Dynamics Istra 4D software to estimate the transient out-of-plane displacement at 2320 spatial points (subset centres) across the plate surface. The primary displacement of interest was the out-of-plane vibration, generating a dataset comprising 2320 spatial points × 4000 temporal steps, equalling over 9 million displacement measurements.

A 3D surface mesh was created from the measured point cloud using Delaunay triangulation [63], accurately capturing the plate’s curvature and enabling detailed geometric and displacement analysis. The specimen and its meshed representation are shown in Fig. 3.

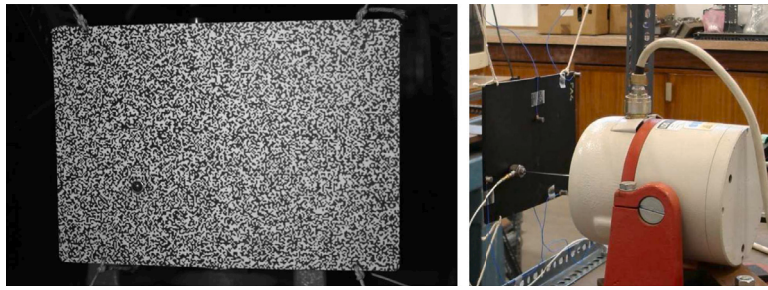


Fig. 2. Left: Front view of the curved plate specimen with a speckle pattern. Right: Back view of the specimen along with the shaker setup.

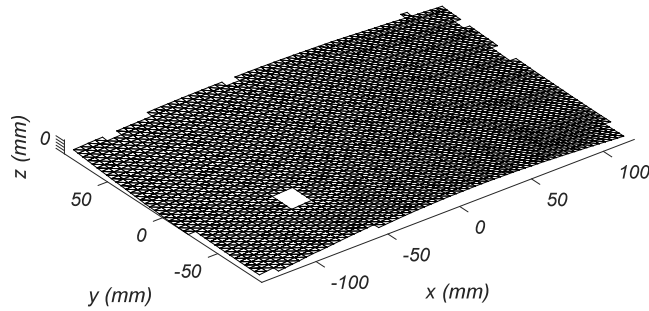


Fig. 3. Specimen of the curved plate presented as a set of DIC meshed triangles.

4.2. Shape basis function construction

To facilitate efficient analysis of the high-dimensional displacement data, a set of orthonormal, data-independent basis functions was constructed directly on the DIC-measured domain using bivariate monomials. These bivariate monomials, spanning from zero to eighth order along the shorter direction of the rectangular specimen and zero to tenth order along the longer direction, were defined over the plate's measured spatial domain. The monomials were orthonormalised using the Gram–Schmidt process to ensure mutual independence, resulting in a total of $R = 99$ orthonormal basis functions.

The full-field dataset, \mathbf{X} , was projected onto the space spanned by the constructed basis functions, forming the AGMD \mathbf{B} , as defined in Eq. (5). The constructed orthonormal basis functions have the dimensions of $\Phi \in \mathbb{R}^{2320 \times 99}$.

Across all temporal samples ($T = 4000$ in this case study), the individual shape's 'energy' as defined in Eq. (7) was estimated by summing the squares of its coefficients over all 4000 temporal sample.

These energy values, $\{E_k, k=1,2,\dots,99\}$, were then used to rank the shape features, retaining the top r basis functions with the highest energy. This selection ensures that the same set of significant features is utilised for all temporal responses. Although the displacement field at different time steps may exhibit varying compression ratios relative to the retained shape feature sets, maintaining consistency in feature selection is crucial for accurate modal identification. Furthermore, quantifying the residual uncertainty arising from the compressed features becomes essential, which is the focus of this paper.

A reduced set of $r = 25$ basis functions was retained to compress the dataset while maintaining high accuracy. The retained number r was determined by ensuring a correlation above a threshold (e.g., 99%) between the original and reconstructed datasets.

The histogram of correlation coefficients between the full-field measured displacements and those reconstructed using 25 AGMD terms is shown in Fig. 4. It can be observed that most correlation coefficients, (ρ , as defined in Eq. (9)), are clustered around 0.999, indicating an excellent approximation for all sampled displacement fields using only 25 AGMD terms to represent 2320 data points.

The most significant 25 basis functions, determined by the magnitude of the AGMD coefficients, are illustrated in Fig. 5. These basis functions exhibit a structured pattern, making them less susceptible to spatial noise. Specifically, the first three functions correspond to vertical tilting, out-of-plane translation, and horizontal tilting, reflecting the plate's fundamental rigid body modes and boundary conditions.

The AGMD method constructs basis functions directly on the measured domain obtained from the DIC system. In principle, orthonormal basis functions can be generated on arbitrary 3D surface meshes, making the method adaptable to structures with complex geometries. While this study focuses on a curved plate, the approach is extendable to other structures, provided that a suitable surface parameterisation is established.

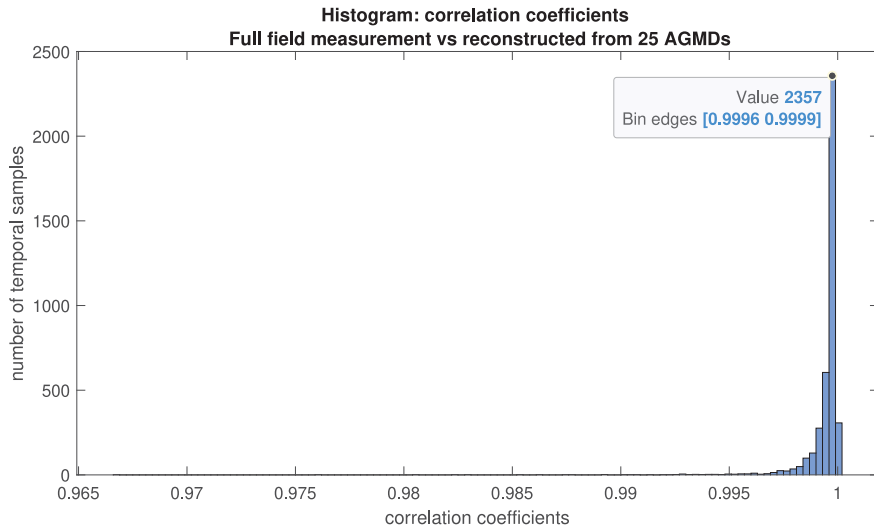


Fig. 4. Histogram of correlation coefficients between full-field measured displacements and those reconstructed using 25 AGMD terms.

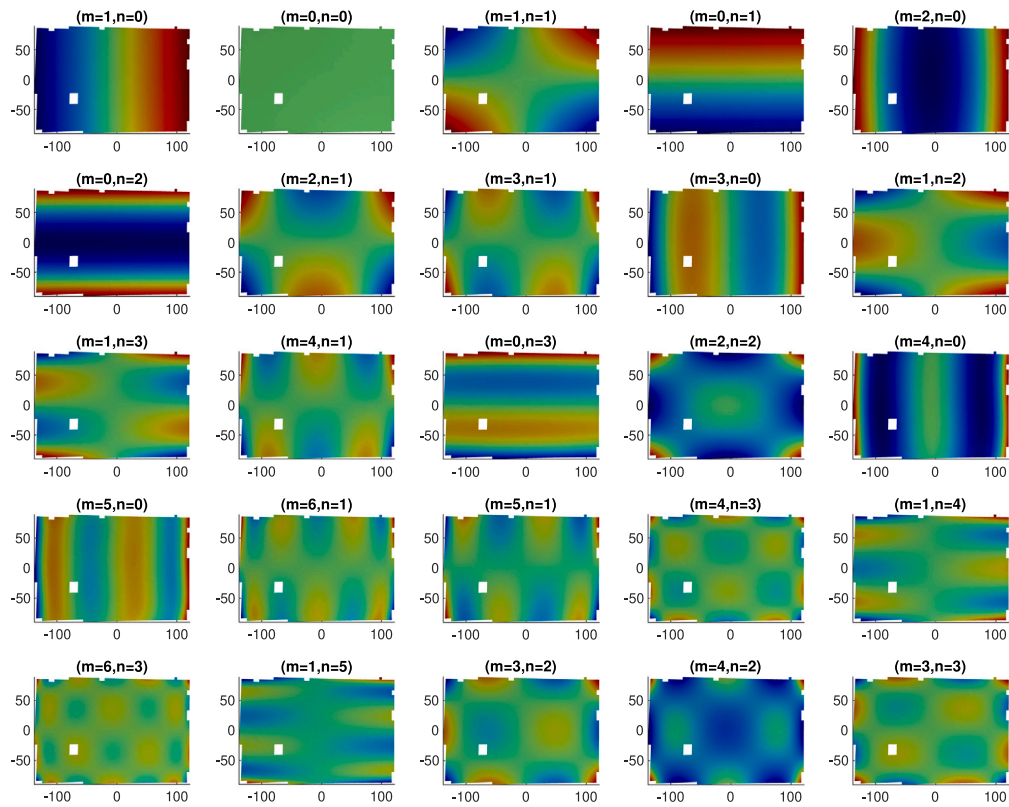


Fig. 5. The most significant 25 orthonormalised monomial basis functions derived from AGMD.

4.3. Modal identification using shape features

With the displacement data compressed into a lower-dimensional feature space using the AGMD, the equation of motion can be transformed into the shape feature space, reducing the system to 25 equations [18]:

$$\tilde{\mathbf{M}}\ddot{\mathbf{b}}(t) + \tilde{\mathbf{C}}\dot{\mathbf{b}}(t) + \tilde{\mathbf{K}}\mathbf{b}(t) = \Phi^T \mathbf{F}(t), \tag{36}$$

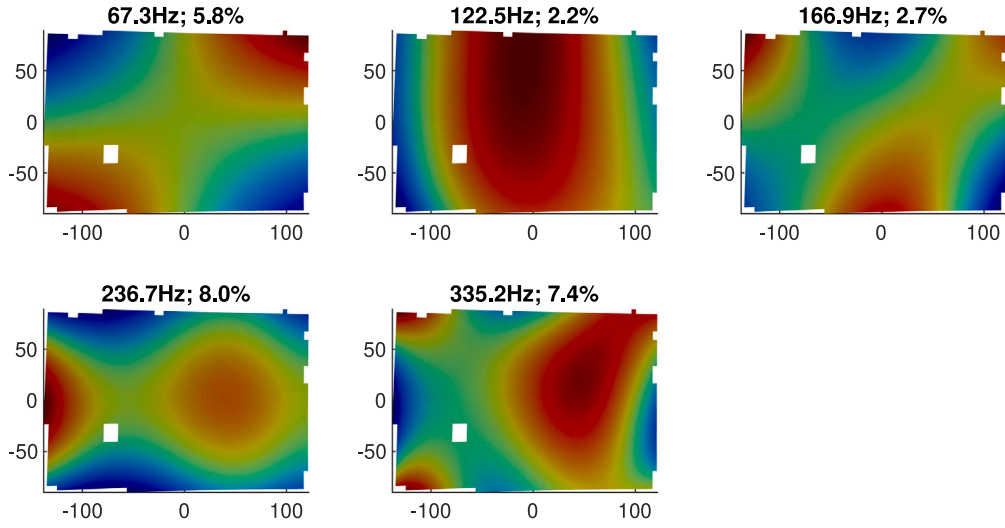


Fig. 6. Reconstructed full-field displacement mode shapes using identified shape feature mode shapes.

where the ‘tilde’ symbol represents the transformed mass, damping, and stiffness matrices in the shape feature space spanned by Φ , while the overhead dot represents the time derivative.

Modal identification was then performed using the time history of shape features (AGMD coefficients) $\mathbf{b} \in \mathbb{R}^r$. The **MATLAB**[®] state-space estimation function `ssrest` [64] was applied to estimate the modal properties from the AGMD data.

Five modes were identified from the AGMD time history, including natural frequencies ω_n , modal damping ratios ζ_n , and AGMD mode shapes \mathbf{u}_n . Notably, the natural frequencies and damping ratios identified in the shape feature space retain their physical meaning as in the original displacement space. For instance, the Frequency Response Function (FRF) expressions in the displacement space and the shape feature space are represented as follows:

In the displacement space [43]:

$$\mathbf{H}_x(\omega) = \sum_{n=1}^{r_s} \frac{\mathbf{v}_n \mathbf{v}_n^T}{\omega_n^2 - \omega^2 + j2\zeta_n \omega_n \omega}, \quad (37)$$

where \mathbf{v}_n are the column vectors of the mode shape matrix \mathbf{V} , and $j = \sqrt{-1}$ denotes the imaginary unit.

In the shape feature space [18]:

$$\mathbf{H}_b(\omega) = \sum_{n=1}^{r_s} \frac{\mathbf{u}_n \mathbf{u}_n^T}{\omega_n^2 - \omega^2 + j2\zeta_n \omega_n \omega}, \quad (38)$$

where \mathbf{u}_n are the column vectors of the shape feature mode shape matrix \mathbf{U} .

These expressions illustrate that the eigenvalues in the denominators, which define the system’s natural frequencies and damping ratios, remain identical in both the displacement and shape feature spaces. The transformation affects only the numerators, which involve the mode shape coordinates, highlighting the preservation of physical meaning in the modal properties across the two spaces.

It can be observed that the shape feature transformation only affects the numerators in the FRF expression, while the eigenvalues in the denominators remain unchanged between the two formulations. This confirms that the natural frequencies and damping ratios identified in the shape feature space would be consistent with those in the displacement space. The full-field displacement mode shapes \mathbf{V} were reconstructed using:

$$\mathbf{V} \approx \Phi \hat{\mathbf{U}}, \quad (39)$$

where $\hat{\mathbf{U}}$ represents the five identified mode shapes in the shape feature space.

The reconstructed mode shapes are shown in Fig. 6, with the corresponding natural frequencies and modal damping ratios indicated in the titles of each subplot. The Auto Modal Assurance Criterion (Auto-MAC) [52] matrix in Fig. 7 confirms the accuracy of the identified modes, with nearly perfect unit diagonal entries.

4.4. Offline empirical covariance estimation

In the offline stage, the empirical covariance matrix was estimated to capture the residual variability not accounted for by the shape feature approximation and modal truncation. The residuals, $\boldsymbol{\eta}$, were computed as the difference between the measured displacement field and the modal approximation. This calculation follows the theoretical framework presented earlier, leveraging the modal expansion and least-squares estimation of modal coordinates (β).

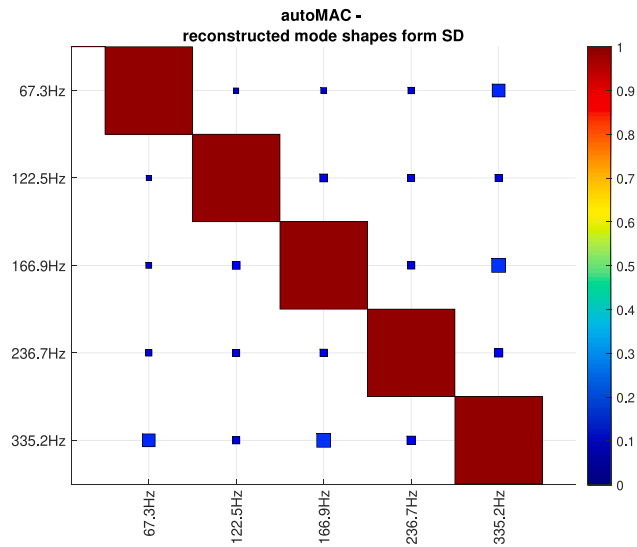


Fig. 7. Auto Modal Assurance Criterion (Auto-MAC) matrix of the identified modes.

The residual covariance matrix, C_η , was estimated based on the sampled displacement field using Eq. (22) in Section 3.2.1. To account for measurement noise, the covariance matrix was adjusted as shown in Eq. (23), isolating the spatially correlated residuals.

Principal Component Analysis was applied to the adjusted covariance matrix, C_η^{adjusted} , yielding a reduced set of residual basis functions (Ψ) and the corresponding variances $\text{diag}(\Lambda)$ along the principal directions. These residual basis functions provide a compact representation of the residuals and were determined to collectively explain 99.95% of the total variance, resulting in six basis functions ($s = 6$) for this case study. These six extracted residual basis functions are visualised in Fig. 8 with their corresponding explained variance λ_i annotated on top of the each subplot.

The empirical covariance structures, illustrated in Fig. 9 for two example locations marked by an asterisk, highlight the spatial correlation of residuals. This eliminates the need to assume a parametric form for the covariance model, such as Exponential or Matérn. The corresponding variance distribution is shown in Fig. 10. These structures play a crucial role in the Kriging-based prediction during the online stage, leveraging spatial correlations in the residuals to enhance full-field reconstruction from sparse sensor measurements.

4.5. Online stage

For the online strategy, a sparse array of point-wise sensors was strategically deployed across the entire field to facilitate the effective reconstruction of the response field from expansion via basis functions. The optimal sensor locations were identified by selecting p rows of the matrix formed by basis functions. This selection ensures that the reduced basis matrix retains the essential spatial characteristics necessary for accurately reconstructing the combination coefficients. Thereby preserving the fidelity of the full-field displacement representation.

4.5.1. QR decomposition with column pivoting

Sensor placement for optimal reconstruction was performed using QR decomposition with column pivoting, as detailed in Section 2.4.1. This approach formalises the selection of sensor locations by identifying rows of the shape basis matrix Φ that maximise their linear independence. The permutation matrix \mathbf{P} generated during the QR decomposition process determines the order of selected locations, prioritising rows that contribute the most to the system’s independence and enhancing the stability of inverting.

In this case study, where $N_d = 2320$ DOFs and $r = 25$ retained shape basis functions, **MATLAB**®’s built-in QR decomposition function was applied to determine $p = r = 25$ optimal sensor locations. The results are shown in Fig. 11, where the blue dot markers indicate the selected locations, and annotated numbers reflect their order as determined by the pivoting algorithm. Notably, the selected locations initially cluster along the outer edges and gradually cover inner regions, achieving a well-distributed coverage across the entire specimen.

Five modes were identified using a conventional subspace identification method on the compressed shape features, accounting for approximately 99.9% of the total shape information. Consequently, 25 AGMD terms were retained to represent the high-resolution displacement field, as shown by the correlation coefficient histogram in Fig. 4. While the number of sensors does not need to match the number of modes, deploying $p = 25$ sensors provides sufficient spatial coverage (spanning over 2000 spatial points) for transient measurements.

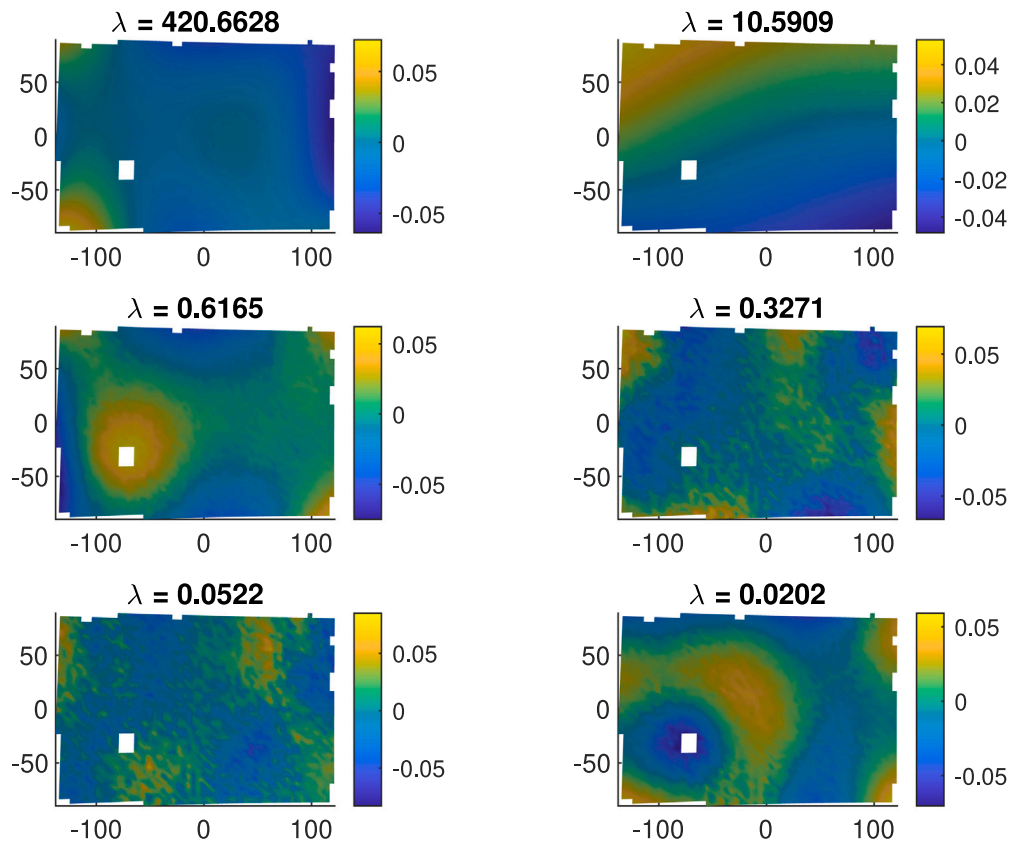


Fig. 8. Residual basis functions: The first six principal components capturing 99.95% of the total residual variance.

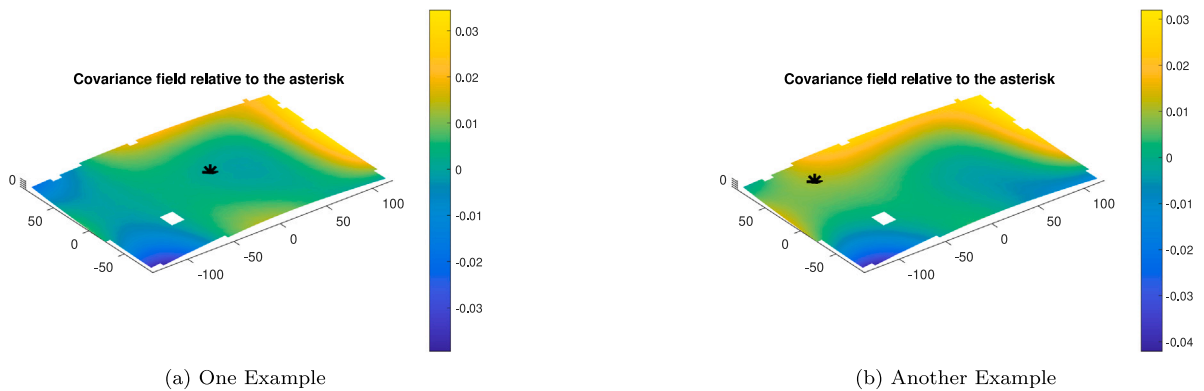


Fig. 9. Covariance field example at selected locations.

In practice, the sensor selection process (using QR decomposition with pivoting) may stop when the next pivot in the R matrix falls below a predefined fraction of the largest pivot. This balances the diminishing returns on measurement information with computational efficiency, allowing a more flexible determination of the sensor count.

Using measurements from these selected sensor locations ($\mathbf{x}_i \in \mathbb{R}^{25}$), the modal coefficients β_i were estimated as per Eq. (30) from Section 3.4.1. This computation involves the reduced matrix $\mathbf{V}_p \in \mathbb{R}^{25 \times 5}$ corresponding to the sensor locations and the observed covariance matrix \mathbf{C}_{obs} , which incorporates the residual basis functions (Ψ_p), their explained variances (Λ), and the measurement noise variance ($\hat{\sigma}^2$).

The ‘point-wise’ sensor responses were derived from the DIC dataset, providing an opportunity to directly compare the reconstructed full-field responses, obtained through the proposed method, with the true displacement fields measured by DIC.

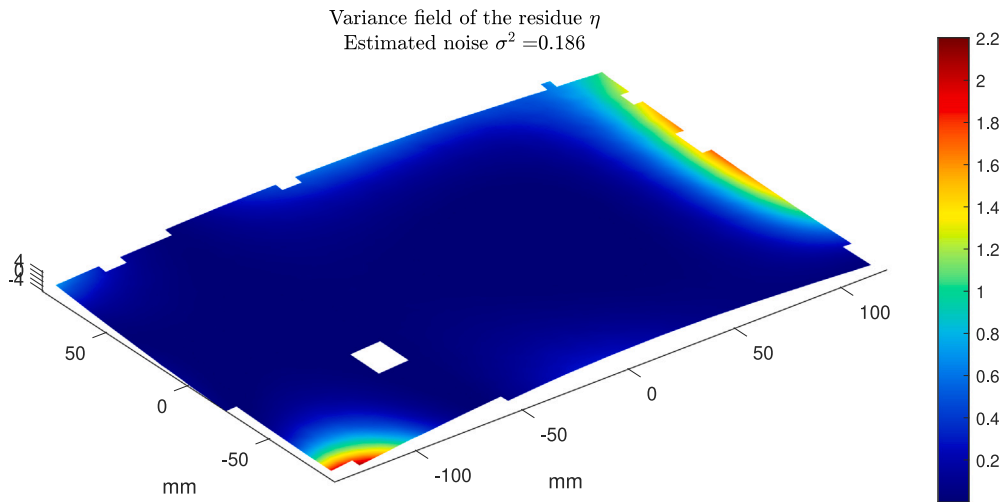


Fig. 10. Variance of residuals (η).

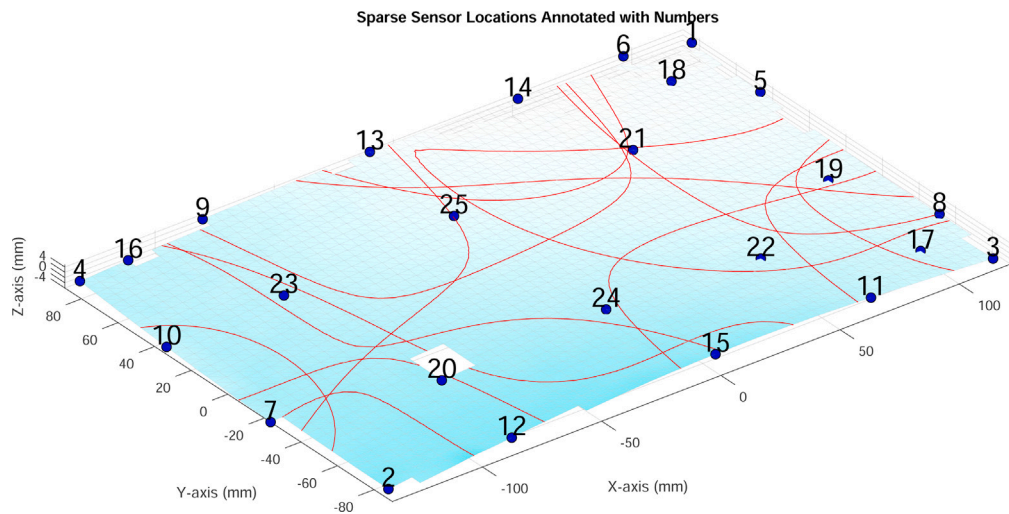


Fig. 11. Optimal sensor locations identified using QR decomposition with 25 sparse sensors, overlaid on the nodal lines of the mode shapes.

This comparison serves to validate the accuracy and robustness of the sensor placement strategy and subsequent reconstruction methodology.

4.5.2. Kriging prediction

After estimating the modal coefficients (β_i), the residuals at the measured sensor locations were calculated as:

$$\mathbf{r}_t = \mathbf{x}_t - \Phi_p \mathbf{U} \beta_t \tag{40}$$

Kriging interpolation was used to predict the residuals ($\eta_{\bar{p},t}$) at unmeasured locations ($S_{\bar{p}}$) based on the residual covariance structure estimated during the offline stage. The joint distribution of the residuals at the measured and unmeasured locations at time t is characterised by the covariance matrices as detailed in Section 3.4.2.

The predicted mean residuals at unmeasured locations ($\mu_{\eta_{\bar{p},t}}$) and their conditional covariance ($\mathcal{V}_{\eta_{\bar{p}}}$) were computed using the conditional distribution formulas by Eqs. (34) and (35), respectively. These computations leverage the spatial correlation captured in the covariance structure to provide accurate predictions and associated uncertainties.

The performance of the Kriging prediction was evaluated by comparing the true full-field measurements with the predicted displacements. Fig. 12 presents this comparison at a representative time sample, including the predicted 95% confidence intervals.

The plot provides a comparative analysis of true versus predicted displacements, incorporating uncertainty quantification for a selected time sample (Time Sample #500). The predictions are obtained from an online stage model, which leverages basis functions and statistical inference to estimate displacements at unobserved points within the structure.

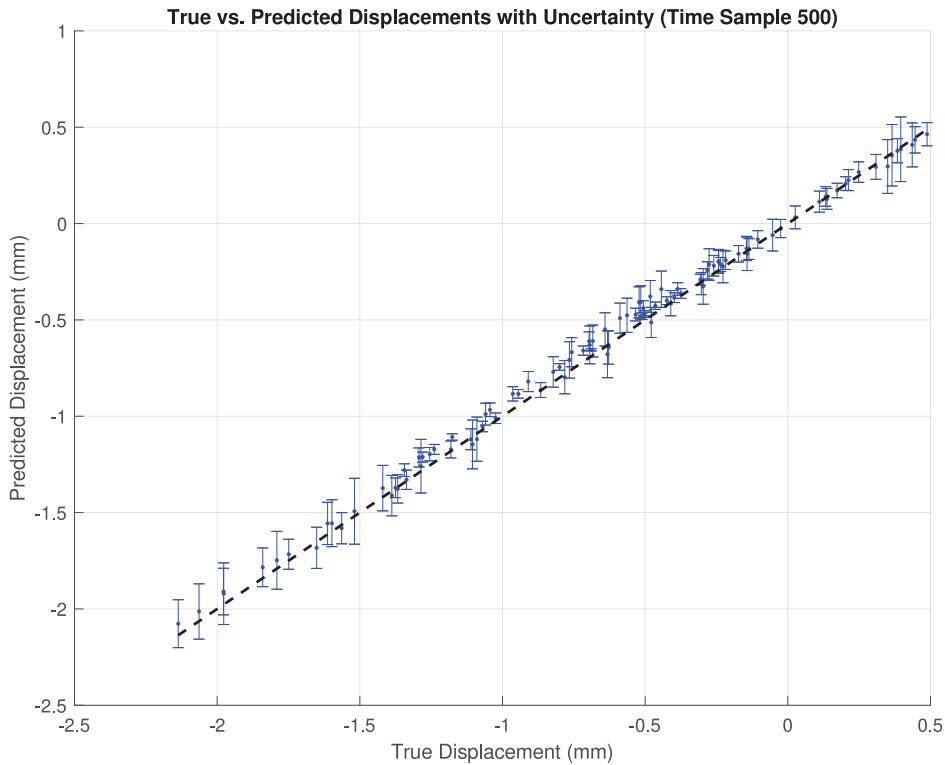


Fig. 12. Comparison between true full-field measurements and Kriging-predicted displacements at one time sample, including 95% confidence error bars.

In this scatter plot, each blue marker represents a selected unobserved point where displacement has been predicted. The vertical blue error bars denote the standard deviation (square root of variance) of the prediction uncertainty, corresponding to a 95% confidence level. The black dashed line represents the ideal prediction scenario, where predicted displacements perfectly match the true displacements.

The predicted values exhibit strong agreement with the true displacements along the ideal 45-degree reference line, demonstrating the model’s effectiveness in capturing the structural response. The uncertainty bars provide insight into the confidence of the predictions, with smaller intervals indicating higher certainty. To enhance clarity in visualisation, only 100 out of a total of 2320 spatial points are displayed in the figure. The majority of the confidence intervals overlap with the 45-degree line, indicating accurate predictions. However, a small number of intervals, particularly around the -0.9mm region, slightly deviate from the ideal line. Nevertheless, the overall distribution of uncertainty intervals remains acceptable.

These results highlight the robustness of the proposed methodology in estimating structural displacements while providing quantified uncertainty. A more detailed comparison of the full field will be presented in the following paragraphs.

Figs. 13 and 14 further illustrate the 95% confidence upper and lower uncertainty bounds derived from the Kriging formulation. While the upper bound consistently covers the entire field, the lower bound marginally undercovers certain regions. Despite this, the narrow gap between the bounds highlights the predictive accuracy and reliability of the Kriging approach, underpinned by the informed empirical covariance estimation conducted during the offline stage.

For this representative time sample, the relative error between the Kriging-predicted full-field response and the true displacement field is visualised in Fig. 15. The majority of the region exhibits minimal relative error below 0.5%, as indicated by the colour bar. The region with higher relative error is concentrated around a small central area, showing approximately 4.5% relative error.

In comparison, Fig. 16 illustrates the relative error between the true displacement and the Generalised Least Squares (GLS) fitted response. While the same central region displays discrepancies, the GLS approach exhibits higher relative differences of 7% or more. The overall relative error across the mesh is also higher, ranging around 1%–2%. These results demonstrate that the Kriging prediction is more informative and accurate, benefiting from the inclusion of the covariance structure from the offline stage.

4.5.3. Validation of the Kriging model

To evaluate the performance of the proposed method comprehensively, the *coverage probability* was assessed as a quantitative metric. Coverage probability measures the proportion of true displacement values that fall within the predicted confidence intervals, providing insight into the calibration and reliability of the model’s uncertainty estimates.

The objective was to evaluate whether the true displacements ($X_{\text{true},t}$) at unmeasured locations are captured within the predicted 95% confidence intervals. For each time sample, a set of $p = 25$ vertices (S_p) was selected as measured locations, and the remaining

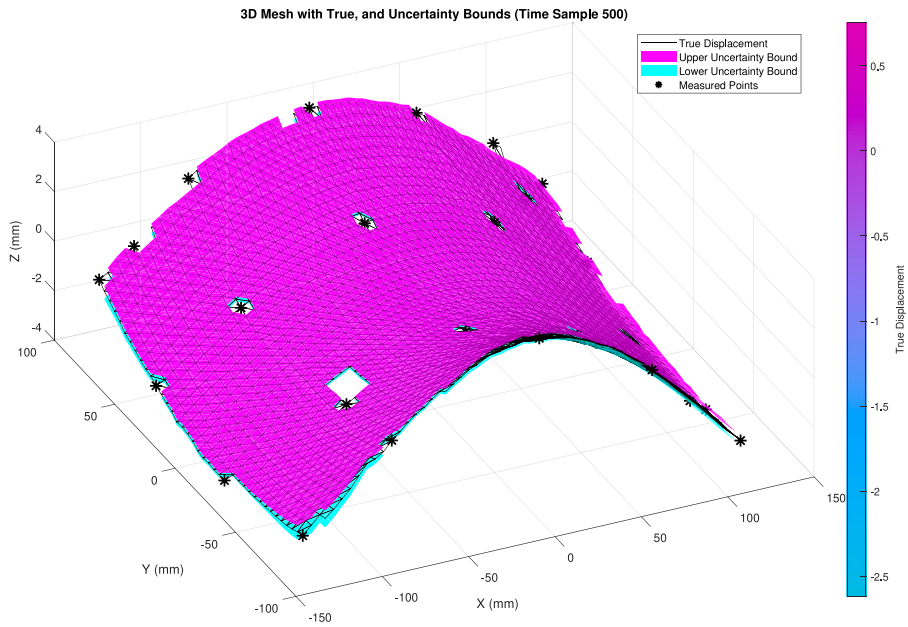


Fig. 13. Comparison between true full-field measurements and Kriging-predicted uncertainty **upper bound** at one time sample.

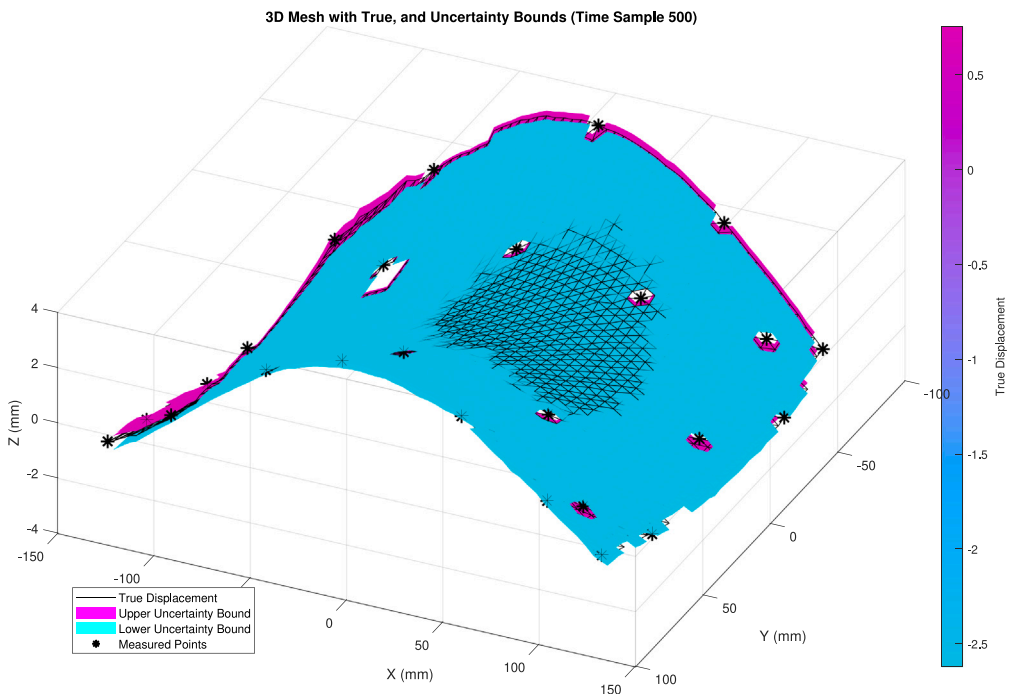


Fig. 14. Comparison between true full-field measurements and Kriging-predicted uncertainty **lower bound** at one time sample.

vertices (S_p) were treated as unmeasured points where predictions were made. At each unmeasured location i , the 95% confidence interval was constructed using the predicted mean displacement ($\hat{X}_{p,t}^{(i)}$) and the associated variance ($\text{Var}_\eta^{(i)}$):

$$\text{Lower Bound} = \hat{X}_{p,t}^{(i)} - z \cdot \sqrt{\text{Var}_\eta^{(i)}} \tag{41}$$

$$\text{Upper Bound} = \hat{X}_{p,t}^{(i)} + z \cdot \sqrt{\text{Var}_\eta^{(i)}} \tag{42}$$

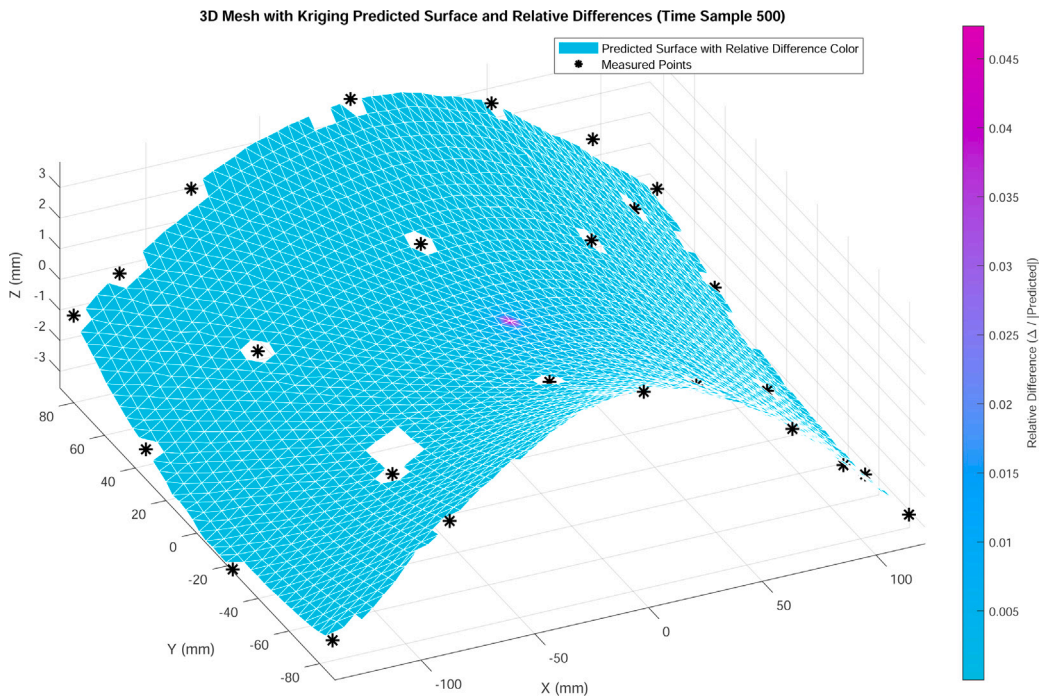


Fig. 15. Relative error between true displacement and Kriging-predicted displacement.

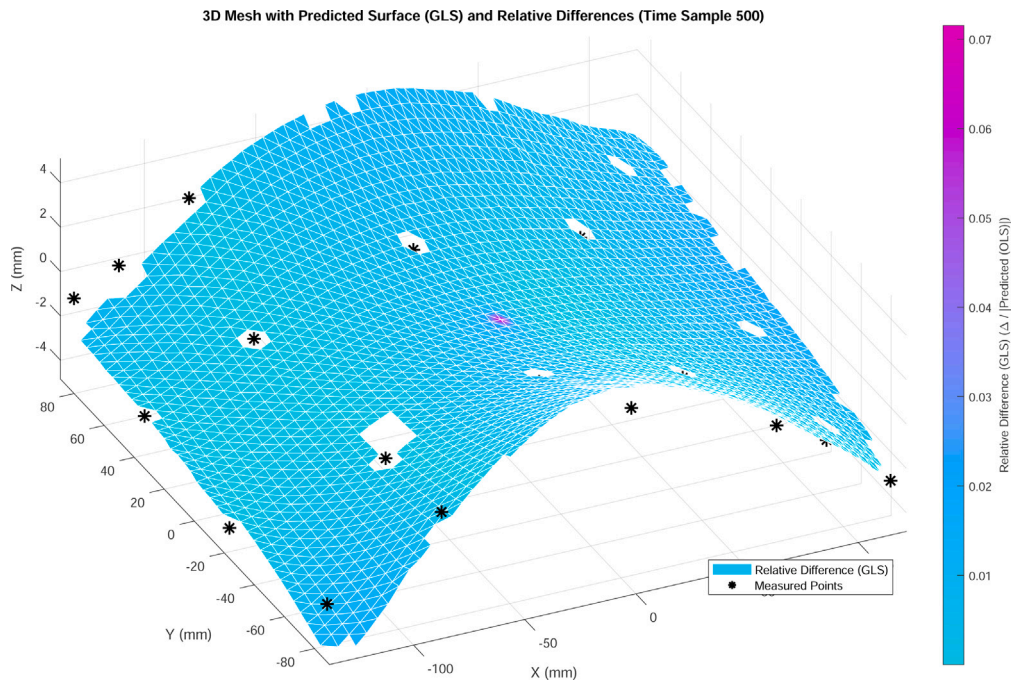


Fig. 16. Relative error between true displacement and GLS-fitted displacement.

where $z \approx 1.96$ corresponds to the 95% confidence level.

For each unmeasured location, the true displacement ($X_{true,t}^{(i)}$) was compared against the confidence interval:

$$\text{Coverage Indicator}^{(i)} = \begin{cases} 1, & \text{if Lower Bound} \leq X_{true,t}^{(i)} \leq \text{Upper Bound} \\ 0, & \text{otherwise.} \end{cases} \tag{43}$$

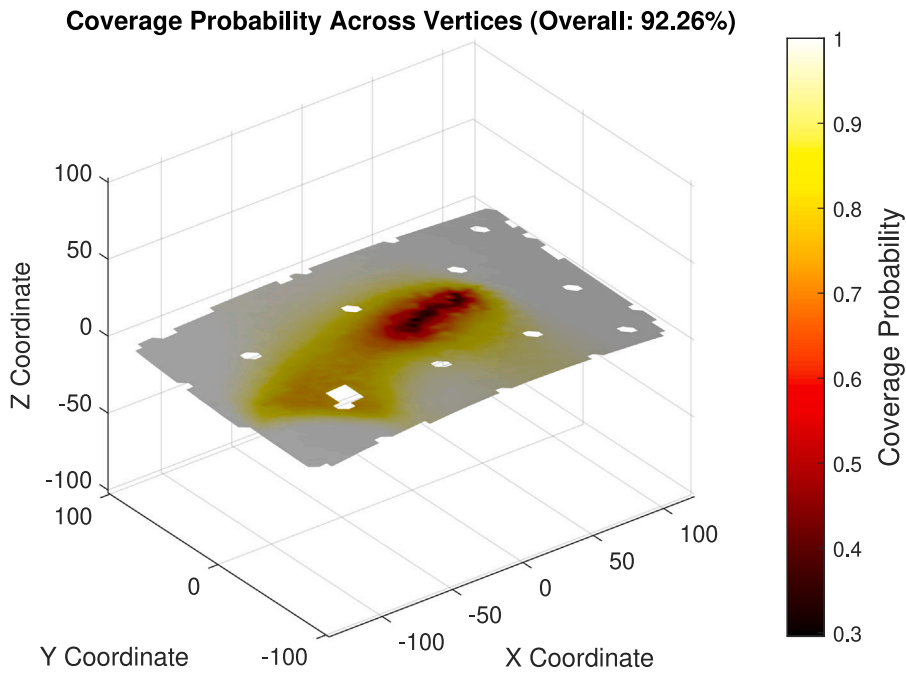


Fig. 17. Coverage probability map using 25 sensors, achieving an overall coverage probability of 92.26%.

The overall coverage probability was then computed as:

$$\text{Coverage Probability} = \frac{\sum_i \text{Coverage Indicator}^{(i)}}{\text{Total Number of Predictions}} \tag{44}$$

This process was repeated across multiple validation time samples, covering all unmeasured locations in the dataset. The results were aggregated to obtain the final coverage probability.

Coverage Probability Results

The effectiveness of the Kriging predictions was evaluated through the coverage probability using 25 sparse sensors across the entire dataset. As illustrated in Fig. 17, the coverage probability was generally high in the outer regions of the plate but exhibited slight undercoverage towards the centre. The overall coverage probability of 92.26% for a nominal 95% confidence interval demonstrates that the Kriging model provides reliable displacement predictions and reasonable uncertainty estimates. The lower coverage observed at central locations can be attributed to the inherently smaller displacement amplitudes (as shown in Fig. 18), resulting in reduced signal-to-noise ratios. To address this, additional sensor locations were introduced, specifically targeting the central region, which subsequently improved coverage from a minimum of 0.30 to 0.55 and raised the overall coverage probability to 94.34% as shown in Fig. 19. This confirms that the sensor placement strategy effectively enhances spatial representation and reliability of the Kriging-based structural response prediction.

4.6. Case study summary

The case study applied the proposed two-stage methodology to the vibration analysis of a curved plate, demonstrating its effectiveness in reconstructing full-field displacements from sparse sensor measurements. In the offline stage, the AGMD reduced dataset dimensionality, while empirical covariance structures were estimated from residuals to inform Kriging-based predictions. Optimal sensor locations were identified using QR decomposition with column pivoting to ensure comprehensive spatial coverage. During the online stage, Kriging accurately predicted residuals at unmeasured locations, enabling precise full-field displacement reconstruction. The method achieved strong agreement with true displacements, at a representative time sample, with relative errors below 0.5% across most regions and a maximum of 4.5% in localised areas. Coverage probability assessment further validated the approach, achieving a reliability of 94.34% for the 95% confidence interval.

5. Conclusion & future work

This paper presents a two-stage methodology that integrates Modal Order Reduction and Kriging for efficient and accurate full-field displacement reconstruction using sparse online measurements derived from high-resolution Digital Image Correlation data. The proposed approach leverages orthonormal shape basis functions, constructed via the Adaptive Geometric Moment Descriptor,

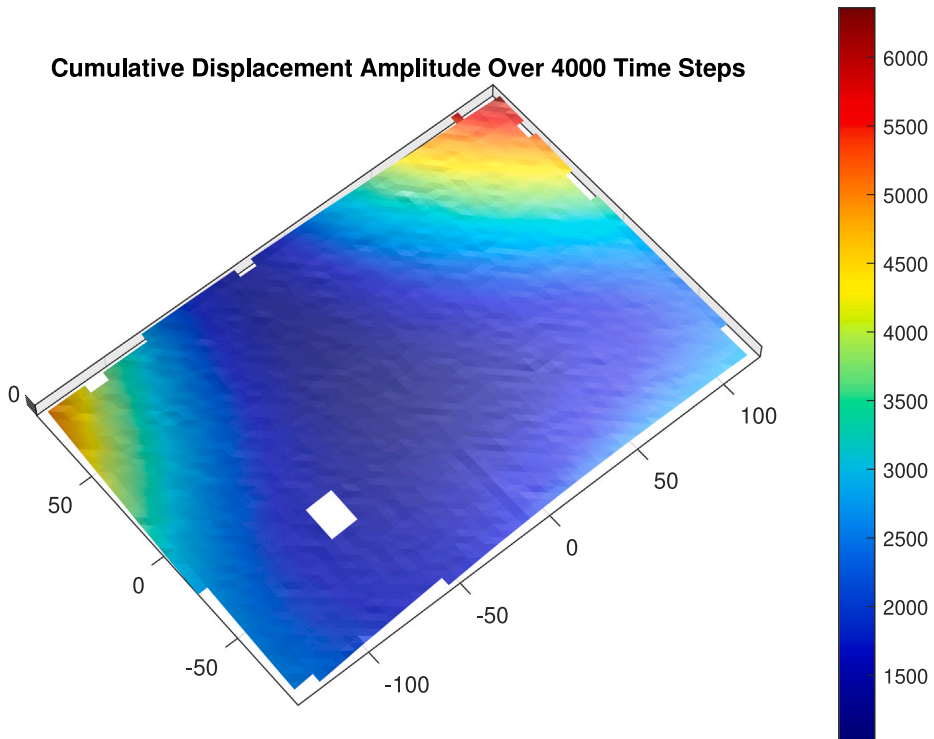


Fig. 18. Cumulative displacement amplitude at each point in the displacement field over the entire measurement history of 4000 temporal time steps.

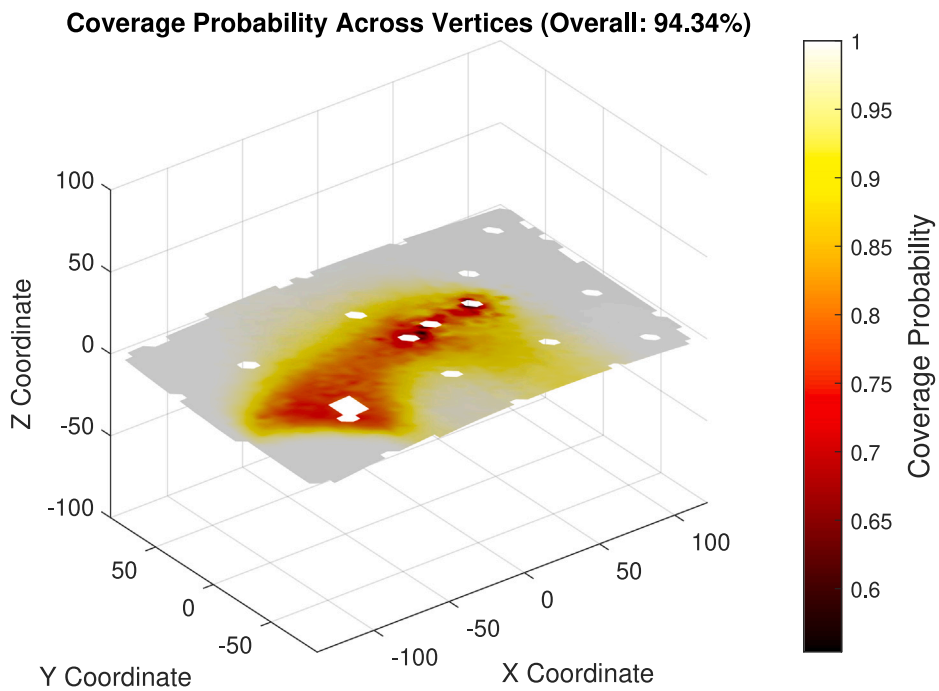


Fig. 19. Coverage probability map incorporating three additional sensors in the central region, compared to Fig. 17. The overall coverage probability increased from 92.26% to 94.34%.

to compress large-scale displacement datasets while preserving essential structural dynamics. Optimal sensor placement is achieved through QR decomposition with pivoting, ensuring high linear independence and enhancing the stability of modal coefficient

estimation. The integration of Kriging interpolation for residual prediction further improves reconstruction accuracy and provides reliable uncertainty quantification, as demonstrated by a coverage probability in the case study of a curved plate. Overall, this data-driven framework proves effective and shows strong potential for robust, scalable applications in structural health monitoring.

While the current two-stage approach provides a robust framework for reconstructing full-field displacements with uncertainty quantification, several avenues remain open for further refinement and extension. Firstly, during the online stage, the methodology could be adapted to estimate the full-field response spectrum. By incorporating spectral analysis techniques into the Kriging-based inference, the method could provide real-time insights into frequency-dependent behaviours, assisting engineers in identifying critical resonance conditions or evolving dynamic features. Secondly, translating the displacement field predictions into strain fields and subsequently deriving strain spectra is not explored. Future studies can focus on building strain estimation models directly from the shape basis functions and the Kriging residual framework. By incorporating uncertainty quantification into the strain spectrum calculations, practitioners can obtain confidence intervals around strain-related parameters, enhancing the reliability of structural health assessments and informing maintenance or retrofit decisions.

Declaration of competing interest

The author declares no conflicts of interest concerning this research or its publication.

Acknowledgements

The author gratefully acknowledges the use of data from the EU project ADVISE (Advanced Dynamic Validations using Integrated Simulation and Experimentation), funded under Grant No. 218595.

Data availability

Data will be made available on request.

References

- [1] O. Avcı, O. Abdeljaber, S. Kiranyaz, M. Hussein, M. Gabbouj, D.J. Inman, A review of vibration-based damage detection in civil structures: From traditional methods to machine learning and deep learning applications, *Mech. Syst. Signal Process.* 147 (2021) 107077, <http://dx.doi.org/10.1016/j.ymssp.2020.107077>.
- [2] C. Farrar, K. Worden, An introduction to structural health monitoring, *Philos. Trans. R. Soc. A: Math. Phys. Eng. Sci.* 365 (1851) (2007) 303–315, <http://dx.doi.org/10.1098/rsta.2006.1928>.
- [3] A. Deraemaeker, E. Reynders, G. De Roeck, J. Kullaa, Vibration-based structural health monitoring using output-only measurements under changing environment, *Mech. Syst. Signal Process.* 22 (1) (2008) 34–56, <http://dx.doi.org/10.1016/j.ymssp.2007.07.004>.
- [4] C. Farrar, K. Worden, Structural health monitoring: A machine learning perspective, 2012, <http://dx.doi.org/10.1002/9781118443118>.
- [5] T. Loutas, A. Bourikas, Strain sensors optimal placement for vibration-based structural health monitoring. The effect of damage on the initially optimal configuration, *J. Sound Vib.* 410 (2017) 217–230, <http://dx.doi.org/10.1016/j.jsv.2017.08.022>.
- [6] C. Niezrecki, J. Baqersad, A. Sabato, Digital image correlation techniques for non-destructive evaluation and structural health monitoring, *Handb. Adv. Non-Destr. Eval.* 46 (2018).
- [7] S. Tchemodanova, M. Sanayei, B. Moaveni, K. Tatsis, E. Chatzi, Strain predictions at unmeasured locations of a substructure using sparse response-only vibration measurements, *J. Civ. Struct. Heal. Monit.* 11 (4) (2021) 1113–1136, <http://dx.doi.org/10.1007/s13349-021-00476-x>.
- [8] A. Kamariotis, E. Chatzi, D. Straub, A framework for quantifying the value of vibration-based structural health monitoring, *Mech. Syst. Signal Process.* 184 (2023) <http://dx.doi.org/10.1016/j.ymssp.2022.109708>.
- [9] J. Mottershead, M. Friswell, Model updating in structural dynamics: A survey, *J. Sound Vib.* 167 (2) (1993) 347–375, <http://dx.doi.org/10.1006/jsvi.1993.1340>.
- [10] J.E. Mottershead, M. Link, M.I. Friswell, The sensitivity method in finite element model updating: A tutorial, *Mech. Syst. Signal Process.* 25 (7) (2011) 2275–2296.
- [11] I. Behmanesh, B. Moaveni, G. Lombaert, C. Papadimitriou, Hierarchical Bayesian model updating for structural identification, *Mech. Syst. Signal Process.* 64–65 (2015) 360–376, <http://dx.doi.org/10.1016/j.ymssp.2015.03.026>.
- [12] T. Chu, W. Ranson, M.A. Sutton, Applications of digital-image-correlation techniques to experimental mechanics, *Exp. Mech.* 25 (1985) 232–244.
- [13] M. Sutton, F. Hild, Recent advances and perspectives in digital image correlation, *Exp. Mech.* 55 (1) (2015) 1–8.
- [14] M. Grédiac, F. Hild, Full-field measurements and identification in solid mechanics, John Wiley & Sons, 2012.
- [15] C. Niezrecki, P.L. Reu, J. Baqersad, D.P. Rohe, DIC and photogrammetry for structural dynamic analysis and high-speed testing, *Handb. Exp. Struct. Dyn.* (2020) 1–70.
- [16] A. Weidner, H. Biermann, Review on strain localization phenomena studied by high-resolution digital image correlation, *Adv. Eng. Mater.* 23 (4) (2021) 2001409.
- [17] D. Jana, S. Nagarajaiah, Data-driven full-field vibration response estimation from limited measurements in real-time using dictionary learning and compressive sensing, *Eng. Struct.* 275 (2023) 115280.
- [18] W. Wang, J.E. Mottershead, T. Siebert, A. Pipino, Frequency response functions of shape features from full-field vibration measurements using digital image correlation, *Mech. Syst. Signal Process.* 28 (2012) 333–347, <http://dx.doi.org/10.1016/j.ymssp.2011.11.023>.
- [19] Y.-H. Chang, W. Wang, J.-Y. Chang, J. Mottershead, Compressed sensing for OMA using full-field vibration images, *Mech. Syst. Signal Process.* 129 (2019) 394–406, <http://dx.doi.org/10.1016/j.ymssp.2019.04.031>.
- [20] M. Tarpo, T. Friis, C. Georgakis, R. Brincker, Full-field strain estimation of subsystems within time-varying and nonlinear systems using modal expansion, *Mech. Syst. Signal Process.* 153 (2021) 107505, <http://dx.doi.org/10.1016/j.ymssp.2020.107505>, URL <https://www.sciencedirect.com/science/article/pii/S0888327020308918>.
- [21] S. Chen, Y. Zheng, F. Wang, E. Cai, Y. Zhang, H. Liu, Z. Qu, Computer vision-based reliability analysis in digital twinning for structural dynamic safety assessment, *Eng. Struct.* 326 (2025) 119532.

- [22] Y. Zhang, R. Hao, J. Niiranen, Y. Yang, E. Brühwiler, D. Su, T. Nagayama, Computational engine for finite element digital twins of structural dynamics via motion data, *Eng. Struct.* 316 (2024) 118630.
- [23] X.H. Zhang, X.Y. Xiao, Z.P. Yang, S.E. Fang, Response reconstruction based on measurement matrix optimization in compressed sensing for structural health monitoring, *Adv. Struct. Eng.* (2024) 13694332241300670, <http://dx.doi.org/10.1177/13694332241300670>.
- [24] Y. Zhang, J. Tang, Unveiling structural integrity through data driven reconstruction, in: *Dynamics, Vibration, and Control of ASME International Mechanical Engineering Congress and Exposition*, vol. 5, 2024, V005T07A060, <http://dx.doi.org/10.1115/IMECE2024-145681>.
- [25] M.S. Floater, K. Hormann, Surface parameterization: a tutorial and survey, *Adv. Multiresolution Geom. Model.* (2005) 157–186.
- [26] F.P. Preparata, M.I. Shamos, *Computational geometry: an introduction*, Springer Science & Business Media, 2012.
- [27] W. Wang, J.E. Mottershead, Adaptive moment descriptors for full-field strain and displacement measurements, *J. Strain Anal. Eng. Des.* 48 (1) (2013) 16–35.
- [28] S.J. Leon, Å. Björck, W. Gander, Gram-Schmidt orthogonalization: 100 years and more, *Numer. Linear Algebra Appl.* 20 (3) (2013) 492–532.
- [29] J. Baqersad, K. Bharadwaj, Strain expansion-reduction approach, *Mech. Syst. Signal Process.* 101 (2018) 156–167, <http://dx.doi.org/10.1016/j.ymssp.2017.08.023>.
- [30] M.A. Mendez, A. Ianiro, B.R. Noack, S.L. Brunton, *Data-driven fluid mechanics: combining first principles and machine learning*, Cambridge University Press, 2023.
- [31] S. Cao, N. Guo, C. Xu, Robust damage localization in plate-type structures by using an enhanced robust principal component analysis and data fusion technique, *Mech. Syst. Signal Process.* 162 (2022) 108091.
- [32] E. Reynders, G. Roeck, Reference-based combined deterministic-stochastic subspace identification for experimental and operational modal analysis, *Mech. Syst. Signal Process.* 22 (3) (2008) 617–637, <http://dx.doi.org/10.1016/j.ymssp.2007.09.004>.
- [33] N. Maia, J. Silva, Modal analysis identification techniques, *Philos. Trans. R. Soc. A: Math. Phys. Eng. Sci.* 359 (1778) (2001) 29–40, <http://dx.doi.org/10.1098/rsta.2000.0712>.
- [34] F.P. Kopsaftopoulos, S.D. Fassois, Vibration based health monitoring for a lightweight truss structure: experimental assessment of several statistical time series methods, *Mech. Syst. Signal Process.* 24 (7) (2010) 1977–1997.
- [35] A. Poulimenos, S. Fassois, Parametric time-domain methods for non-stationary random vibration modelling and analysis—a critical survey and comparison, *Mech. Syst. Signal Process.* 20 (4) (2006) 763–816.
- [36] K. Worden, *Nonlinearity in structural dynamics: detection, identification and modelling*, CRC Press, 2019.
- [37] I. Jamaludin, N. Wahab, N. Khalid, S. Sahlan, Z. Ibrahim, M. Rahmat, N4SID and MOESP subspace identification methods, 2013, pp. 140–145, <http://dx.doi.org/10.1109/CSPA.2013.6530030>.
- [38] L. Ljung, State of the art in linear system identification: Time and frequency domain methods, 1, 2004, pp. 650–660, <http://dx.doi.org/10.23919/acc.2004.1383678>,
- [39] J.-H. Yi, C.-B. Yun, Comparative study on modal identification methods using output-only information, *Struct. Eng. Mech.* 17 (3–4) (2004) 445–466, <http://dx.doi.org/10.12989/sem.2004.17.3.4.445>.
- [40] W.-X. Ren, G. De Roeck, Structural damage identification using modal data. I: Simulation verification, *J. Struct. Eng.* 128 (1) (2002) 87–95, [http://dx.doi.org/10.1061/\(ASCE\)0733-9445\(2002\)128:1\(87\)](http://dx.doi.org/10.1061/(ASCE)0733-9445(2002)128:1(87)).
- [41] B. Peeters, G. De Roeck, Reference-based stochastic subspace identification for output-only modal analysis, *Mech. Syst. Signal Process.* 13 (6) (1999) 855–878, <http://dx.doi.org/10.1006/mssp.1999.1249>.
- [42] M. El-Kafafy, P. Guillaume, B. Peeters, Modal parameter estimation by combining stochastic and deterministic frequency-domain approaches, *Mech. Syst. Signal Process.* 35 (1–2) (2013) 52–68, <http://dx.doi.org/10.1016/j.ymssp.2012.08.025>.
- [43] D.J. Ewins, *Modal testing: theory, practice and application*, John Wiley & Sons, 2009.
- [44] P. Van Overschee, B. De Moor, N4SID: Subspace algorithms for the identification of combined deterministic-stochastic systems, *Automatica* 30 (1) (1994) 75–93, [http://dx.doi.org/10.1016/0005-1098\(94\)90230-5](http://dx.doi.org/10.1016/0005-1098(94)90230-5).
- [45] L. Ljung, *System identification*, in: *Signal Analysis and Prediction*, Springer, 1998, pp. 163–173.
- [46] Z. Lai, I. Alzugaray, M. Chli, E. Chatzi, Full-field structural monitoring using event cameras and physics-informed sparse identification, *Mech. Syst. Signal Process.* 145 (2020) <http://dx.doi.org/10.1016/j.ymssp.2020.106905>.
- [47] T. Sibert, T. Becker, K. Spillthof, I. Neumann, R. Krupka, High-speed digital image correlation: Error estimations and applications, *Opt. Eng., Bellingham* 46 (5) (2007) <http://dx.doi.org/10.1117/1.2741217>.
- [48] M. Helfrick, C. Niezrecki, P. Avitabile, T. Schmidt, 3D digital image correlation methods for full-field vibration measurement, *Mech. Syst. Signal Process.* 25 (3) (2011) 917–927, <http://dx.doi.org/10.1016/j.ymssp.2010.08.013>.
- [49] T. Siebert, M.J. Crompton, Application of high speed digital image correlation for vibration mode shape analysis, in: *Application of Imaging Techniques To Mechanics of Materials and Structures, Volume 4: Proceedings of the 2010 Annual Conference on Experimental and Applied Mechanics*, Springer, 2012, pp. 291–298.
- [50] D.C. Kammer, Sensor placement for on-orbit modal identification and correlation of large space structures, *J. Guid. Control Dyn.* 14 (2) (1991) 251–259, <http://dx.doi.org/10.2514/3.20635>.
- [51] B. Chen, Z. Huang, D. Zheng, L. Zhong, A hybrid method of optimal sensor placement for dynamic response monitoring of hydro-structures, *Int. J. Distrib. Sens. Networks* 13 (5) (2017) 1550147717707728.
- [52] R.J. Allemang, The modal assurance criterion—twenty years of use and abuse, *Sound Vib.* 37 (8) (2003) 14–23.
- [53] F.E. Udvardi, Methodology for optimum sensor locations for parameter identification in dynamic systems, *J. Eng. Mech.* 120 (2) (1994) 368–390, [http://dx.doi.org/10.1061/\(asce\)0733-9399\(1994\)120:2\(368\)](http://dx.doi.org/10.1061/(asce)0733-9399(1994)120:2(368)).
- [54] C. Papadimitriou, Optimal sensor placement methodology for parametric identification of structural systems, *J. Sound Vib.* 278 (4–5) (2004) 923–947, <http://dx.doi.org/10.1016/j.jsv.2003.10.063>.
- [55] A.M. Kosikova, O. Sedeji, C. Papadimitriou, L.S. Kataygiotis, Bayesian structural identification using Gaussian process discrepancy models, *Comput. Methods Appl. Mech. Engrg.* 417 (2023) 116357.
- [56] C. Yang, H. Ouyang, A novel load-dependent sensor placement method for model updating based on time-dependent reliability optimization considering multi-source uncertainties, *Mech. Syst. Signal Process.* 165 (2022) 108386.
- [57] K. Manohar, B.W. Brunton, J.N. Kutz, S.L. Brunton, Data-driven sparse sensor placement for reconstruction: Demonstrating the benefits of exploiting known patterns, *IEEE Control Syst. Mag.* 38 (3) (2018) 63–86.
- [58] A. Saito, T. Kuno, Data-driven experimental modal analysis by dynamic mode decomposition, *J. Sound Vib.* 481 (2020) <http://dx.doi.org/10.1016/j.jsv.2020.115434>.
- [59] Z. Drmac, S. Gugercin, A new selection operator for the discrete empirical interpolation method—improved a priori error bound and extensions, *SIAM J. Sci. Comput.* 38 (2) (2016) A631–A648, <http://dx.doi.org/10.1137/15m1019271>.
- [60] N. Cressie, *Statistics for spatial data*, John Wiley & Sons, 2015.
- [61] A.E. Gelfand, P. Diggle, P. Guttorp, M. Fuentes, *Handbook of spatial statistics*, CRC Press, 2010.
- [62] N. Cressie, G. Johannesson, Fixed rank kriging for very large spatial data sets, *J. R. Stat. Soc. Ser. B Stat. Methodol.* 70 (1) (2008) 209–226, <http://dx.doi.org/10.1111/j.1467-9868.2007.00633.x>.
- [63] F. Aurenhammer, Voronoi diagrams—a survey of a fundamental geometric data structure, *ACM Comput. Surv.* 23 (3) (1991) 345–405, <http://dx.doi.org/10.1145/116873.116880>.
- [64] L. Ljung, *System identification toolbox: User's guide*, Citeseer, 1995.